

# Surface Waves in the Western Taiwan Coastal Plain From an Aftershock of the 1999 Chi-Chi, Taiwan, Earthquake

November 30, 2005

by Guo-Quan Wang, Guo-Qing Tang, David M. Boore, G. Van Ness Burbach,  
Caesar R. Jackson, Xi-Yuan Zhou, and Qing-Liang Lin

Corresponding author and mailing address:

Guo-Quan Wang

Applied Geophysical Science Laboratories

North Carolina A & T State University

1020 East Wendover Ave., Room 003

Greensboro, NC 27411

Phone: 336-256-2100

Fax: 336-256-2102

E-mail: gwang@ncat.edu

## Abstract

Significant surface waves were recorded in the western coastal plain (WCP) of Taiwan during the 1999 Chi-Chi, Taiwan, earthquake and its series of aftershocks. We study in detail the surface waves produced by one aftershock (09/20/99, 18:03:41.16, **M** 6.2) in this paper. We take the Chelungpu-Chukou fault to be the eastern edge of the WCP, because it marks a distinct lateral contrast in seismic wave velocities in the upper few kilometers of the surface. For many records from stations within the WCP, body waves and surface waves separate well in both the time domain and the period domain. Long-period (e.g.,  $> 2$  sec) ground motions in the plain are dominated by surface waves. Significant prograde Rayleigh wave particle motions were observed in the WCP. The observed peak ground velocities are about 3 to 5 times larger than standard predictions in the central and western part of the plain. Observed response spectra at 3 sec, 4 sec, and 5 sec at the center of the plain can be 15 times larger than standard predictions, and 10 times larger than the predictions of Joyner (2000) based on surface-wave data from the Los Angeles basin. The strong surface waves were probably generated at the boundary of the WCP, and then propagated towards the west, largely along radial directions relative to the epicenter. The geometry of the boundary may have had a slight effect on propagation directions of surface waves. Group velocities of fundamental-mode Rayleigh and Love waves are estimated using the Multiple Filter Analysis (MFA) technique and refined with the Phase Matched Filtering (PMF). Group velocities of fundamental-mode surface waves range from about 0.7 km/sec to 1.5 km/sec for the phases at periods from 3 sec to 10 sec. One important observation from this study is that the strongest surface waves were recorded in the center of the plain. The specific location of the strongest motions depends largely on the period of surface waves, rather than on specific site conditions or plain structures. Accordingly, we conjecture that surface waves could be generated in a wide area close to boundaries of low velocity sedimentary waveguides. In the case studied in this article, the area can be as wide as 30 km (from the Chelungpu fault to the center of the plain). Surface waves converted by *P*- and *S*-waves at different locations would overlap each other and add constructively along their propagation path. As a result, the surface waves would get stronger and stronger. Beyond a certain distance to the boundary, no more surface waves would be generated. Consequently no more local surface waves would be superimposed into the invasive surface waves,

and the surface waves would tend to decay in amplitude with distance.

## Introduction

It is widely recognized that surface waves (including Love waves and Rayleigh waves) make an important contribution to long-period strong ground motions from earthquakes. In particular, the motions in sedimentary waveguides can be dominated by the surface waves locally generated by the conversion of body waves at the margins of the waveguides (Boore *et al.*, 1971; Liu and Heaton, 1984; Vidale and Helmberger, 1988; Graves *et al.*, 1998; Boore, 1999a; Field *et al.*, 2000; Joyner, 2000; Hartzell *et al.*, 2003; Kawase, 1996; Rovelli *et al.*, 2001; Cornou *et al.*, 2003; Iida and Kawase, 2004; Graves and Wald, 2004; Frankel *et al.*, 2001). Field (1996) reported that amplification factors associated with surface waves as measured by sediment-to-bedrock spectral ratios can reach as high as 18 at some frequencies.

Strong ground motions observed in sedimentary waveguides are normally a mixture of body waves (*P*- and *S*-waves) and surface waves. In small true basins, the short travel time of surface waves, complexities of boundary geometry, multiple reverberations between borders, and overlapping of multi-pathing surface waves along their propagation can result in a very complex surface wave field, which superimpose upon body wave arrivals. Generally, it is difficult to separate body waves and surface waves from strong ground-motion records, particularly from near-source records. Hence, it would be difficult to do specific studies on surface waves using strong ground-motion records from small basins. In contrast, a portion of Taiwan is an excellent natural laboratory for studying surface waves, for several reasons: 1) there is a blanket of sediments extending west of an essentially north-south trending boundary between the sediments and basement rocks to the east of the sediments; 2) the region is well instrumented with digital strong-motion recorders of the Taiwan Strong-Motion Instrumentation Program (TSMIP) (Shin and Teng, 2001), with an average distance between neighboring stations in the plain of about 5 km; 3) the 1999 Chi-Chi mainshock and its series of aftershocks with magnitude of about **M** 6.0 were well recorded on the network of instruments.

The western coastal plain (WCP) of Taiwan is filled with Quaternary sediments about 2 km thick

(e.g., Stach, 1958; Hsiao, 1971; Teng, 1990; Satoh *et al.*, 2001; Wen and Chen, 2004). Buried beneath the sediment is a complex composed primarily of pre-Tertiary igneous and metamorphic rocks (Lu *et al.*, 2002). There are a sequence of thrust faults under the plain (e.g., Suppe, 1981; Davis *et al.*, 1983). A major pre-Miocene basement high, the Peikang high, is found beneath the coastal plain. The highest part of the basement high is in the vicinity of Peikang at a depth of about 1500 m (Tang, 1977). (see Figure 1 for the location of Peikang). At the north-west edge of the plain are the Pakua and other tablelands and the Taichung piggyback basin. Late Quaternary fluvial sediments in this basin reach thicknesses of 3 km (Chang, 1971). There are several sub-parallel, north trending thrust faults separated by about 20 km. The westernmost (the Changhua fault) might be taken as the eastern boundary of the WCP, but it penetrates Quaternary sediments near the surface, while the more eastern one (the Chelungpu-Chukou fault, on which the mainshock occurred) forms a more distinct boundary between the lower velocity materials extending to the west and the bedrock of the mountains to the east. For this reason, we take the Chelungpu-Chukou fault as the eastern boundary of the WCP in this study (as do Shin and Teng, 2001). Figure 2 shows a very simple geologic profile across the WCP.

In this study, site conditions are classified according to the average  $S$ -wave velocity of the top 30-meter of sediments ( $\bar{V}_s(30)$ ) in keeping with current NEHRP (National Earthquake Hazard Reduction Program) standards (BSSC 1995, 1998, 2001; Dobry *et al.*, 2000). Measured shear-wave velocities, based on measurements using the suspension  $P - S$  logging method (see <http://geo.ncree.org.tw>) are available at the majority of stations in our study area (between  $23^\circ$  and  $24.5^\circ$  north latitude) that recorded the Chi-Chi mainshock and aftershocks (Figure 1). We use the  $\bar{V}_s(30)$  values in the PEER NGA database (<http://peer.berkeley.edu/nga/>). The values include those derived from the suspension log measurements as well as those estimated at stations for which suspension log values are not available presently; the estimated values are based on correlations between local geologic descriptors and  $\bar{V}_s(30)$  established from data in Taiwan and California.

In this article, we study the surface waves produced by an aftershock that occurred on 20 September, 1999, at 18:03 (UTC) with a magnitude of  $M$  6.2, which was named as aftershock 1803 by Lee *et al.* (2001). The main reason that we select event 1803 in this study is that it produced stronger surface waves in the plain than other aftershocks. Figure 1 shows the locations of the epicenter and 250

free-field stations from which the records triggered by this event are available from Lee *et al.* (2001). Figure 1 also presents locations of Chelungpu-Chukou (heavy dark lines), Changhua-Chiuchunkun (gray lines) faults and the epicenters of the Chi-Chi mainshock and five aftershocks mentioned in this article. The epicenters, origin times and main source parameters of these events are listed in Table 1.

Figure 3 illustrates some acceleration and displacement time series (east-west component) observed in the WCP during event 1803. It is clear that ground motions in the plain include obvious late-arriving, long-period motions. The late arrival of these waves, their significant amplitudes, and their long-period characters, as well as their elliptical polarization of particle motion (studied in detail later), suggest that they are surface waves. Similar surface waves are also observed during some other aftershocks of the Chi-Chi event as shown in Figure 4. The three column shows the acceleration, velocity, and displacement time series (radial directions relative to corresponding epicenters) from these five aftershocks and the mainshock at station CHY025 (marked in Figure 3). Figure 4 indicates there are significant surface waves in the records from events 1803 and 2352, as well as in records from events 0014 and 2146. The reason why event 1803 produced stronger surface waves than the other four events in the plain may be complex. Compared with other aftershocks, its epicenter is closer to the boundary of the plain (17 km), its hypocenter is shallower (about 8 km), and its fault dip is smaller (only  $10^\circ$ ). These factors may have produced stronger body waves at the edge of the sedimentary waveguide, which combined with a shallower incidence angle may have resulted in more efficient conversion into surface waves.

Because of the ease of development on the coastal plain and the proximity of the plain to the epicentral area of the Chi-Chi earthquake and its aftershocks, the strong surface waves are of great interest in engineering concerns. The main purpose of this study is to document the existence of the surface waves propagating across the plain and investigate the change of amplitude with the distance from an engineering viewpoint; no attempt is made to do simulations of the waves.

## Data

The free-field ground-motion data used in this work are from the Central Weather Bureau of Taiwan Strong-Motion Data Series CD-002 distributed by Lee *et al.* (2001). In order to study long-period surface waves, the acceleration data are integrated to displacement traces. In our previous studies (e.g., Boore, 1999b; Boore, 2001a; Wang *et al.*, 2001; Wang *et al.*, 2003; Wang *et al.*, 2004), we found that almost all recordings from the Chi-Chi event and its aftershocks were plagued by random baseline offsets, which have a significant effect on the integrated displacement time series. The baseline offsets impact only very long period information, fortunately. An important conclusion from our previous work is that high and middle frequency (e.g.,  $> 0.05$  Hz) information, of concern to us in this paper, is nearly unaffected by specific baseline corrections. Accordingly, a simple baseline correction scheme is applied to the acceleration data before calculating the displacement time series in this study.

Most records from the TSMIP instruments have a pre-event portion which is very important for controlling the baseline (zero-line) of the record. The length of the pre-event portion is 20 sec for most TSMIP records. Firstly, the mean of the pre-event portion is removed from the whole record. For those records without the pre-event portion or the pre-event portion less than 10 sec, the mean of the whole trace is removed. Then an acausal, fourth-order Butterworth, low-cut filter with corner frequency of 0.05 Hz is applied to the whole record (acceleration time series). The two processes effectively eliminate the problems caused by the baseline offsets. The displacement time series integrated from the corrected record should be a good representation of the actual ground displacement for surface waves with periods somewhat less than about 15 sec. Unless otherwise stated, “ground motions” hereinafter refer to the displacement time series processed with the above baseline correction scheme.

## Separation of Body Waves and Surface Waves: An Example

Late-arriving surface waves distinguish themselves mostly by their long-period and large-amplitude features in accelerograms and displacement diagrams as shown in Figure 3. As an example, we show the three-component acceleration time series, as well as their corresponding Fourier amplitude spectra observed at station CHY025 in Figure 5a. The original horizontal components (east-west and

north-south, simplified as EW and NS in this article) have been rotated into the radial and transverse components relative to the epicenter. The backazimuth between the epicenter and station CHY025 is  $85^\circ$ . The first 20 sec of the each trace is the pre-event portion. The *P*-wave arrives at about 20-sec and the surface wave arrives at about 30-sec. The late-arriving surface wave overlaps with the body wave for about 2-4 sec (e.g., from 30 to 34 sec). After that, the ground motions are dominated by long-period motions. Based on these observations, we separate each trace into two segments: body wave (from 20-30 sec) and surface wave (from 30 to 70 sec).

In Figure 5b, we compare 5%-damped pseudovelocity (PSV) response spectra calculated from the body wave segment (20-30 sec), the surface wave segment (30-70 sec), and the whole trace (0-70 sec). Enough zeros have been padded to the beginning and the end of the body-wave and surface-wave segments before calculating the PSV to account for the filter transients (e.g., Boore, 2005). It is clear that the response spectra of the surface waves are much larger than those from the body waves at middle and long periods (e.g.,  $> 1$  sec). At the periods around the peak response of the surface wave segment (about 3-4 sec), the PSVs from the surface wave are about 9, 4 and 10 times larger than those from the body wave for the radial, transverse and vertical components, respectively. The PSV curve of the whole trace can be separated into two segments: a short-period segment ( $< 0.5$  sec) corresponding to the body waves, and a long-period segment ( $> 0.5$  sec) controlled by the surface waves. It seems that the body and surface waves recorded at this station separate well in both the time and period domains.

Particle motion plots (“hodograms”) are a compact way of viewing information about seismic particle motions (e.g., Boore *et al.*, 2004). To see the particle motions produced by the body waves and surface waves, we plot the hodograms from station CHY025 in the plane of Rayleigh wave propagation (Figure 6). Figures 6a and 6b show the horizontal and vertical acceleration and displacement traces of the Rayleigh waves. Figures 6c and 6d are the hodograms for the acceleration and displacement respectively. Sub-figures at their right side are the hodograms of body wave motions (0-20 sec, 20-27 sec, and 27-30 sec) and Rayleigh wave motions (30-38 sec, 38-50 sec, and 50-60 sec). These hodograms of the Rayleigh wave generally show a dominant polarization oriented approximately  $45^\circ$  to the wave propagation direction.

There is a remarkable jump in both the acceleration and displacement hodograms of the 0—20-sec segment at about 19.6 sec. The sudden jump indicates the arriving of the earliest seismic wave (*P*-wave). The polarization of the acceleration hodogram changes suddenly around 27 sec from the vertical to horizontal directions. Correspondingly, the path of the particle motion changes from anti-clockwise (prograde) to clockwise (retrograde). The sudden change of the polarization probably indicates the arrival of the *S*-wave. The particle motion changes back to anti-clockwise around 30 sec, and changes to clockwise again near 38 sec. The particle motions after 38 sec are a well-developed series of retrograde ellipses, as we anticipate for Rayleigh waves. However, the particle motions from 30 to 38 sec, which are the strongest segment of the acceleration trace, are not retrograde elliptical motions but prograde elliptical motions. This phenomenon is mainly caused by very slow shallow velocities underlying the plain. Based on a theoretical analysis, Tanimoto and Rivera (2005) concluded that if there exists a thick sedimentary layer with extremely slow seismic velocities, Rayleigh wave particle motion can become prograde near the surface. An observation of the prograde elliptical motion is difficult in practice, because particle motion is largely horizontal and high microseismic noise exists in the same frequency band. Fortunately, significant prograde Rayleigh wave particle motions were recorded in the plain mainly because this earthquake is very close to the sediment plain.

## Generation of Surface Waves

Ground-motion studies in California (Liu and Heaton, 1984; Vidale and Helmberger, 1988; Graves *et al.*, 1998; Boore, 1999b; Joyner, 2000; Hartzell *et al.*, 2003) and other regions (Kawase, 1996; Rovelli *et al.*, 2003; Cornou *et al.*, 2003; Iida and Kawase, 2004), as well as many numerical simulations (e.g., Boore *et al.*, 1971; Komatitsch *et al.*, 2004) have concluded that surface waves can be generated from the conversion of body waves at margins of low velocity sedimentary waveguides. In this section, we will give an example to show that the surface waves can be generated at places very close to the boundary of the sedimentary waveguide. Figure 7 shows the displacement phases with different periods of horizontal Rayleigh waves (EW component) observed at stations TCU129,



TCU076, TCU122 and CHY026. Specific locations of these stations are marked in Figure 3. Station TCU129 is located very close to the boundary of the plain (horizontal distance to the boundary [ $R_B$ ] is about 1.5 km); station TCU076 is a little bit farther ( $R_B = 2.5$  km); and station TCU122 is located about 9 km away from the fault ( $R_B = 9$  km). Station CHY026 is located at the center of the coastal plain, about 30 km away from the Chelungpu-Chukou fault ( $R_B = 30$  km). We select these stations because they are in a small range of latitude relative to the epicenter, so that their east-west components are approximately in the radial direction of the surface wave propagation. Therefore, the long-period motions (e.g.,  $> 2$  sec) of the east-west (EW) component would be dominated by Rayleigh waves.

The displacement time series (EW component) from these stations are shown in Figure 7a. We extract phases at periods of 3 sec, 5 sec, and 7 sec from these displacement traces using the Multiple Filter Analysis (MFA) techniques (Dziewonski *et al.*, 1969). In Figure 7b, the peaks of envelopes of different phases arrive at the same time, which implies that there is no phase dispersion in the record of TCU129. In Figure 7c, the peak of the 3-sec envelope is about 2 sec later than that of the 5-sec envelope, which suggests that there is a slight phase dispersion in the record of TCU076. The change of phase dispersion with frequency is also called “envelope delay” (e.g., Boore, 2003). It is clear that there are significant envelope delays in the Rayleigh waves of TCU122 (Figure 7d) and CHY026 (Figure 7e). It appears that the envelope delays increase with the distance to the plain boundary ( $R_B$ ). Furthermore, it seems that the amplitudes of phases also increase with the increment of  $R_B$ . The amplitudes of these phases at periods of 3 sec, 5 sec, and 7 sec of CHY026 ( $R_B = 30$  km) are about 1.5 times of those from TCU122 ( $R_B = 9$  km), which in turn are about 1.5 times of those from TCU076 ( $R_B = 2.5$  km) and TCU129 ( $R_B = 1.5$  km). These observed phase dispersions suggest that the surface waves originate even before station TCU076 ( $R_B = 2.5$  km).

There are two possibilities why there is no phase dispersion in the record of TCU129 ( $R_B = 1.5$  km). One is that there are no surface waves in the record at all (only body waves), and thus there is no phase dispersion. The other possibility is that there are surface waves in the record, but phase-dispersion is difficult to discern because the travel-distance is too short. To investigate this, we compare the ground motions inside and outside the plain. Figure 8a illustrates the vertical

displacement traces of stations TCU129, TCU076, and TCU079. Station TCU079 is located outside of the plain (see Figure 3). It is clear that there are significant late-arriving, long-period motions in the records of TCU129 and TCU076 that are not in the record of TCU079. Figure 8b illustrates the normalized Fourier amplitude spectra of these records. The spectra of these records are roughly comparable in the high frequency range from 0.5 to 2 Hz. However, the spectra of TCU129 and TCU076 are much larger than those of TCU079 in the low frequency range from 0.15 to 0.3 Hz. It is certain that there are long-period surface waves in the record of TCU129 ( $R_B = 1.5$  km). That means surface waves can be produced even before station TCU129. Based on the preceding analyses, we can conclude that surface waves could be generated in the region very close to the boundary (e.g.,  $R_B < 1.5$  km) of the plain. Frequency spectra illustrated in Figure 8b also imply that surface waves are significant only at lower frequencies (e.g., 0.15 to 0.3 Hz, or 3 to 7 sec).

Figure 7f shows the Rayleigh wave phase at 2 sec extracted from the record of CHY026 (Figure 7a). It is clear that the wave is composed of coupled wave-trains, which were generated at different places by  $P$  and  $SV$  conversions. The wave-trains are not as clear in these longer-period phases as in the 2-sec trace because the longer-period phases propagate much faster, so that the distances between different wave-trains are smaller and harder to be seen. The surface waves generated at different places could overlap each other along their propagation. We think the superposition of multi-pathing wave-trains is the main reason why the amplitudes of the surface waves increase with the increment of  $R_B$ . We will discuss this later based on more observations (see section Amplitude and Attenuation of Surface Wave).

## Direction of Surface Wave Propagation

One of the key characteristics of Rayleigh waves is elliptical polarization in the wave propagation plane as shown in Figure 6d. A method of calculating the backazimuth (measured clockwise from north) of the Rayleigh waves has been developed by Chael (1997), Selby (2001) and Baker and Stevens (2004). Its basic idea is to find an azimuth for which the vertical and Hilbert-transformed radial component particle motions form a straight line. We use this method to calculate the

backazimuth of the Rayleigh wave propagation in this work. The first step is to rotate the two horizontal components into assumed radial and transverse directions with a trial backazimuth range from 0 to 360°. Then the radial component is Hilbert-transformed. The Hilbert-transformation has the effect of shifting the horizontal waveform by 90°, which converts the elliptical polarization of the Rayleigh wave into linear motions. The next step is to calculate the cross-correlation between the vertical and Hilbert-transformed horizontal traces with the following formula

$$C_{z\bar{r}} = \frac{S_{z\bar{r}}}{\sqrt{S_{zz}S_{\bar{r}\bar{r}}}}, \quad (1)$$

where  $S_{jk} = \sum_1^n x_j(i)x_k(i)$ ,  $j, k = z, \text{ or } \bar{r}$ .  $x_z(i)$  and  $x_{\bar{r}}(i)$  represent the vertical and Hilbert-transformed horizontal signals (displacements), respectively. The largest cross-correlation corresponds to the best backazimuth of the Rayleigh wave propagation. The backazimuth estimate is controlled by the orientation of the maximum correlation between the horizontal and vertical signals.

One problem is that Equation (1) will return nearly constant values in a large band around the best backazimuth as shown in Figure 9a. For most of records studied in this work, the numerator changes in sync with the second term of the denominator as the algorithm steps through the backazimuth. This makes it difficult to determine an accurate backazimuth. Baker and Stevens (2004) experienced the same problem with noise-free data. To avoid the problem described above, they used another index

$$C_{z\bar{r}} = \frac{S_{z\bar{r}}}{S_{zz}}. \quad (2)$$

We find that Equation (2) is a useful index to get the correct backazimuth. However, Equation (2) does not represent the cross-correlation of the vertical and horizontal Rayleigh waves anymore. The value calculated from Equation (2) can be larger than 1.0. In Equation (1),  $C_{z\bar{r}}$  equalling zero (or very close to zero) indicates the worst correlation between the vertical and horizontal components. In this case, the horizontal component would be Love waves, since Love waves are theoretically independent of Rayleigh waves. The backazimuth of horizontal Rayleigh wave would be in the normal direction of Love wave. Accordingly, we can also get the direction of surface wave propagation from the backazimuth corresponding to the zero-correlation. Since the numerators of Equation (1) and

Equation (2) are the same, they yield zero-correlation at the same backazimuth as shown in Figure 9a. The backazimuth minus  $90^\circ$  corresponds to the peak value of Equation (2). Accordingly, we can decide the wave propagation direction according to the backazimuth obtained from Equation (2). We find this method does not work well for records close to the boundary of the coastal plain, because the phases at different model branches with different polarizations do not separate well within a small propagation distance. However, it works quite well for most of the records about 40 km away from the boundary of the plain.

Figure 9 shows the processing of the backazimuth measurement. The location of station TCU118 is marked in Figure 3. Figure 9a shows curves corresponding to equations (1) and (2). Figure 9b shows vertical and Hilbert transformed horizontal Rayleigh wave traces, as well as the horizontal Rayleigh wave trace. Figure 9c shows original three-component (NS, EW, and Vertical) bandpass-filtered (3–7 sec) displacement traces. The two horizontal components are a mixture of the Rayleigh and Love waves. To separate the Rayleigh and Love waves, the two horizontal components have been rotated  $117^\circ$  (measured clockwise from north), which is the desired backazimuth obtained according to Equation (2). Figure 9d shows the radial and transverse components. The vertical and radial traces clearly show a Rayleigh wave. There is an obvious Love wave in the transverse trace. It seems that the horizontal Rayleigh wave is stronger than the Love wave.

Since a surface wave trace normally includes different modes and multi-pathing waves with different polarizations, the calculated backazimuth is an average value, in turn the wave propagation direction should be regarded as an average of the waves propagating in the dominate direction. Figure 10 plots the directions of Rayleigh wave propagations at 16 stations determined according to the backazimuths obtained from Equation (2). It seems that these surface waves propagate basically along the radial direction relative to the epicenter, which suggests that the boundary geometry had only a slight effect on the propagation direction of the surface waves. According to our plots showing in Figure 3, *P*-waves arrive at about 20 sec and surface waves arrive at about 30–35 sec of these records. To eliminate the effects of body waves and higher mode surface waves, we use the segment from 35 to 70 sec of each record in the calculations. It is difficult to identify exact surface-wave arrivals at these stations. Fortunately, we find that the errors in surface-wave arrivals have a very

slight effect on the final result of Equation (2).

Frankel *et al.* (1991) used a small triangular array to study ground motions in the Santa Clara Valley from aftershocks of the Loma Prieta earthquake. They found that backazimuths are quite different than the backazimuths to the earthquake epicenters, implying scattering from different parts of the basin. The result shown in Figure 10 argues against this being the case in the Western Coastal Plain, which can be regarded as an open-sided basin. It is bounded on the east by the Chelungpu-Chukou fault, which extends roughly in north-south direction. It is open to the west, the slope of the continental shelf as are the Taiwan Straits. The shallower part of the Taiwan Straits is only about 100 meters. The scattering from different parts of the plain would be slight. Multiple reverberations from borders of the plain would also be very slight. Accordingly, the boundary of the plain had only a slight effect on the direction of surface wave propagation in the horizontal plane. Nevertheless, it had a large effect on the propagation of body waves in the vertical plane.

## Surface-Wave Dispersion and Group Velocity

In Figure 7 we showed that the Rayleigh waves propagate from the margin (TCU129,  $R_B = 1.5$  km; TCU076,  $R_B = 2.5$  km; and TCU122,  $R_B = 9$  km) to the center of the plain (CHY026,  $R_B = 30$  km). To see the propagation in the whole plain from east to west, we show the Rayleigh wave phases (vertical) at periods from 2 sec to 8 sec at three illustrated stations CHY024 ( $R_B = 9$  km), CHY002 ( $R_B = 28$  km) and CHY027 ( $R_B = 42$  km) in Figure 11. The locations of these stations are marked in Figure 3. The top subfigure illustrates the Rayleigh waves (vertical) from these stations. Note that these traces have been aligned according to absolute UTC times. It is clear that the Rayleigh wave propagates from east-to-west, crossing station CHY024, CHY002, and CHY027, respectively. There is a clear trend that the amplitudes of long-period Rayleigh phases (from 3 to 7 sec) observed at station CHY002 ( $R_B = 28$  km) are even larger than those observed at station CHY024 ( $R_B = 9$  km). Later, we will show that the attenuation of surface wave is negative in the eastern part of the plain. The phase dispersion decreases with the increase of the period because long-period phases propagate faster than short-period phases. Using the time corresponding to the “envelope delay” and the distance between

two stations, we can estimate the group velocity of the Rayleigh wave. The estimated group velocities are about 0.7 km/sec, 1.2 km/sec, and 1.4 km/sec for vertical Rayleigh waves at 3 sec, 5 sec, and 7 sec respectively, which are comparable with the average group velocities calculated in next section (see Figure 13).

Group velocities of fundamental-mode Rayleigh and Love waves are estimated using the Multiple Filter Analysis (MFA) technique and refined with Phase Matched Filtering (PMF). A Gaussian filter with peak amplitude centered at the desired period is applied to the displacement traces in the frequency domain. The peak of the envelope of the corresponding time domain signal is used to estimate the group travel time. In practice, the true period represented in the filtered signal may not correspond to the Gaussian filter's center period. To account for possible bias produced by changing spectral amplitude, an instantaneous period is measured at the time of the envelope peak. This technique has been used widely in seismology to invert the shear-wave velocity distribution of the Earth's crust (e.g., Goforth and Herrin, 1979; Koch and Stump, 1996; Bonner and Herrin, 1999).

In this study, we use the program “do\_mft” included in the *Computer Program in Seismology* developed by Dr. Herrmann (2002) of Saint Louis University. In the program, the default initial location of a surface wave is set as the location of earthquake epicenter. According to our study, however, the earliest surface waves originated at the boundary of the plain, which is about 17 km away from the epicenter. We modify the program so that the earliest surface waves start at the Chelungpu-Chukou fault in our calculations. Figure 12 presents an example output from the MFT and PMF analysis using the program “do\_mft”. The input recording is the radial component of CHY026 (See Figure 7a). Station CHY026 is located near the center of the coastal plain ( $R_B = 30$  km). Figure 12a illustrates the group-velocity dispersion curve of the horizontal Rayleigh waves. The group-velocity dispersion curve overlaps with contours of amplitude in the period vs. group velocity domain. Figure 12b is the same as Figure 12a, except the Rayleigh wave trace has been corrected with a phase matched filter to isolate the fundamental mode before applying the MFT.

We find it is difficult to get fundamental-mode group velocities with a high resolution for records obtained at stations close to the Chelungpu-Chukou fault (e.g.,  $R_B < 30$  km) because the dispersions of different modes are small. However, the dispersion is much larger for records observed at the

western part of the coastal plain. Accordingly, we only select records from 16 stations located on the west side ( $R_B > 30$  km) of the plain (see Figure 10) to estimate average group velocities of the fundamental-mode surface wave. Original NS and EW components are rotated into the radial and transverse directions. Figure 13 illustrates average group velocities ( $U$  and  $U \pm \sigma$ ) of the fundamental-mode Love and Rayleigh waves. The group velocities change roughly from 0.7 km/sec to 1.5 km/sec for periods from 3 sec to 10 sec, which are similar to the group velocities observed in the Los Angeles Basin by Joyner (2000). He reported that late-arriving surface waves with group velocities around 1 km/sec dominate the ground motion for periods of 3 sec and longer. It seems that the group velocity of the vertical Rayleigh wave is larger than that of the horizontal Rayleigh wave in general, which in turn is larger than that of the Love wave at periods ranging from 3.5 to 10 sec. It also seems that the group velocities of the vertical Rayleigh wave have large variations at long-periods (e.g.,  $> 7$  sec) than the horizontal Rayleigh and Love waves.

The absolute times for each record are very important in calculating the group velocity of surface waves. We use corrected record-start times included in the data files released by Lee *et al.* (2001). They corrected the initial times based on reliable absolute times from some stations with GPS timing devices and an updated velocity structure of Taiwan. The resolution of the time correction is 1 sec for the accelerographs at epicentral distances less than 50 km, and 2 sec for the accelerographs at epicentral distances from 50 to 100 km. The records that we select to calculate the average group velocities are in the range of 30 km to 70 km from the epicenter. Assuming the group velocities of the surface waves are about 1 km/sec, the surface waves generated at the eastern margin of the plain need about 30 sec to reach the center of the plain and 50 sec to reach the west side of the plain. Accordingly, the error in the record-start times would have a very slight effect on the calculated average group velocities shown in Figure 13.

## Cumulative energy

In order to study the proportion of Rayleigh waves and Love waves included in these near-source strong surface waves, we calculate cumulative energy carried by the Love and Rayleigh waves in

the entire ground motions (displacement time series). Wave energy,  $E$  in Joules per square meter, is related to the variance of ground-surface displacement  $z$  by:

$$E = \rho v g \bar{z}^2, \quad (3)$$

where  $v$  is volume of the unit particle;  $\rho$  is density of material at surface;  $g$  is gravity; and  $\bar{z}$  denotes a time or space average of ground surface displacements. The cumulative energy  $E_{Total}$  of the entire seismogram is calculated from the following equation:

$$E_{Total} = \rho v g \sum_{t=1}^n (x(t)^2 + y(t)^2 + z(t)^2) dt. \quad (4)$$

Figure 14 show the area of the Western Coastal Plain studied in this paper. Records from 90 stations (40 C-sites,  $360 < \bar{V}_s(30) < 760$  m/sec; 46 D-sites,  $180 < \bar{V}_s(30) < 360$  m/sec; 4 E-sites,  $\bar{V}_s(30) < 180$  m/sec) are available in the plain for aftershock 1803. We calculate cumulative energy over time of Rayleigh and Love wave traces from these 90 stations. Original NS and EW components of these records are bandpass filtered (a low-cut filtering with corner frequency of 0.05 Hz and a high-cut filtering with frequency of 1 Hz) and rotated into radial and transverse components. The low-cut filtering is used to eliminate the effect of baseline offset problem as we mentioned early; the high-cut filtering is use to remove body waves. The radial and transverse components should be dominated by the Rayleigh and Love waves, respectively, since we have nocited that these surface waves generally propagate in the radial direction (see Figure 10). We use the segment from 30 to 70 sec of each record in the calculations.

Figure 15 shows the ratios of energy carried by Love and Rayleigh waves to total energy carried by the ground motions. It seems that the proportion of energy carried by the Love or Rayleigh waves is independent of the site condition and the distance. The average values of  $E_{Love}/E_{Total}$ ,  $E_{Rayleigh-H}/E_{Total}$ , and  $E_{Rayleigh-V}/E_{Total}$  are 42%, 44% and 14%, respectively. These statistical results are comparable with the results of Cornou *et al.* (2003), who studied the basin surface waves in the Grenoble Basin (French Alps) observed during a total of 18 (6 local, 4 regional, and 8 teleseismic) small and middle earthquakes. They found the surface wave field is composed of 60% Rayleigh waves



and 40% Love waves. If only the energy of horizontal components is considered, this proportion becomes 50% Rayleigh waves and 50% Love waves, on average. Note that most stations that they used are much farther away from the epicenters than those in this paper, and also the amplitudes of surface waves in their study are much smaller than those we used.

## **Amplitude and Attenuation of Surface Waves**

To assess quantitatively the impact of the surface waves on the amplitude of ground shaking, we compare observed peak ground velocities (PGVs) and response spectra with those obtained from “standard” ground-motion prediction equations (GMPEs) currently used in engineering practice. These GMPEs are mostly based on data from body waves. Our previous study (Wang *et al.*, 2004) showed that the ground motions (PGAs, and PSAs within 5 sec) observed outside the plain during event 1803 and other four aftershocks (see Table 1) compare well with the motions from the GMPEs of Abrahamson and Silva (1997), Boore *et al.* (1997), Campbell (1997, 2000, 2001), and Sadigh *et al.* (1997), which were largely based on data (mostly body waves) from California. In this section we check to see if this is also true for motions recorded in the Western Coastal Plain.

In Figure 3, we showed that the amplitudes of the late-arriving surface waves are very significant. We find most PGVs and PGDs (peak ground displacements) are carried by the surface waves in the coastal plain. PGV and PGD represent middle and long-period ground-motion information. Figure 16 shows the spatial distribution of the horizontal PGA, PGV, and PGD recorded in Taiwan during event 1803. These peak values are from low-cut (0.05 Hz) filtered records. The horizontal peaks are the geometric means of the two horizontal values. It is clear that the sediments have a larger effect on PGD and PGV than on PGA.

For many years, researchers have recognized the importance of high-amplitude, long-period ground-motion values in deep sedimentary basins (e.g., Hanks, 1975; Liu and Heaton, 1984; Boore, 1999b; Field *et al.*, 2000). Campbell (1997, 2000) included a term involving depth to basement rock in his equations for predicting long-period response spectra values. His predictions were updated in 2003 (Campbell and Bozorgnia, 2003) based on more observed data. We compare the PGVs and

long-term period response spectra from all stations in the plain (Figure 14), with the predictions of Campbell (1997, 2000, 2003). Figure 17a illustrates the PGVs observed from these stations vs. the predictions of Campbell (1997, 2000). The predictions are for generic soil sites. The C-site PGVs are roughly comparable with the predictions. D- and E-site PGVs are systematically larger than C-site PGVs, and they are significantly larger than the predictions. Figure 17b is the same figure for the Chi-Chi mainshock (**M** 7.6). In contrast to the aftershock, the observed PGVs from the mainshock are generally comparable to the predicted values. Although not shown here, we note that the PGAs of the mainshock are considerably smaller than the predictions in general (Boore, 2001b; Wang *et al.*, 2002). Our interpretation of the comparisons in Figure 17 is that the PGVs of the mainshock are carried mostly by body waves, while the PGVs of the aftershock are carried mostly by surface waves (see Figure 4 for records from an illustrated station).

In Figure 18, we compare 5%-damped pseudoacceleration (PSA) responses at 3 sec and 4 sec observed in the plain with the predictions of Campbell and Bozorgnia (2003). The predictions are for generic soil sites. Both horizontal and vertical PSAs at C sites are slightly larger than the mean-plus-one-standard-deviation predictions in general. The PSAs at D and E sites are systematically larger than those at C sites for both the vertical and horizontal components. Observed PSAs can be as much as 10 times larger than the predictions at the peak response.

Abrahamson and Silva (1997) made a special effort to extract long-period signals from strong-motion recordings; therefore, their equations probably contain a greater contribution from surface waves than these equations developed by other researchers (e.g., Boore *et al.* 1997; Sadigh *et al.* 1997). In Figure 19, we compare the 5%-damped pseudovelocity (PSV) responses at 3 sec, 4 sec, and 5 sec observed in the coastal plain with the predictions from Abrahamson and Silva (1997). The agreement between observations at class C sites and soil-site predictions is somewhat better than it was for the Campbell and Bozorgnia predictions shown in Figure 18, but this could be simply coincidence. Generic soil sites are probably more similar to NEHRP class D sites than class C sites (Boore and Joyner, 1997; W. Silva, personal communication), and as in Figure 18, the observed motions on class D sites are significantly above the predicted soil motions.

Figure 19 also compares the observed motions with the predictions of Joyner (2000). Joyner's

predictions are for strong motions triggered by surface waves. The amplitude of ground motion is modeled by the expression

$$\log y = f(\mathbf{M}, R_E) + c + bR_B , \quad (5)$$

where  $y$  is the PSV spectrum,  $f(\mathbf{M}, R_E)$  is a ground-motion prediction based on a general strong-motion data set (we used the GMPE of Abrahamson and Silva [1997]),  $\mathbf{M}$  is the moment magnitude,  $b$  is a parameter controlling the attenuation with distance within the plain, and  $c$  is a measure of coupling between the incident body waves and the surface waves in the plain.  $R_E$  is the distance from the source to the boundary of the plain, and  $R_B$  is the distance from the boundary to the recording site. Joyner pointed out that his equation gives median estimates of the motions that may exceed the estimates from attenuation relationships based on the general strong motion data set by a factor of three or more for the same source-site distances. The observed motions in the WCP, however, are much larger than the predictions of Joyner (2000). In the center of the coastal plain the observations exceed the predictions of Joyner by a factor of 10 for the vertical and “perpendicular” components (the latter being the direction of motion roughly perpendicular to the boundary of the WCP, for which we use the EW component) and by a factor of 3 for the “parallel” component of motion (for which we use the NS component).

One direct observation from Figure 17a, Figure 18, and Figure 19 is that the long-period ground motions (e.g.,  $> 2$  sec) at the D and E sites are systematically stronger than those at the C-sites; this is the usual result found in empirical studies of ground motions (e.g., Boore *et al.*, 1997), but as mentioned before, those studies probably included few records for which surface waves controlled the longer-period amplitudes. Thus the amplification of the class D and E sites relative to the class C sites might be due to something in addition to different near-site conditions. The amplifications also seem to be related to the distance from these sites to the boundary of the plain ( $R_B$ ). As Figure 14 shows, the C sites are preferentially closer to the boundary than the D and E sites, and thus a dependence on distance to the boundary ( $R_B$ ) would be mapped into an apparent site class dependence. Iida and Kawase (2004) reported that surface waves are found to be much more heavily amplified than S-waves in soft deposits. It is possible that these softer D and E sites have a large amplification on

the surface waves coming from these harder C sites, and that the local site response is less significant than amplifications related to the distance traveled from the edge of the WCP (as discussed later). In Figure 17a, Figure 18, and Figure 19, we show that the PGV and PSVs from four E-site stations are comparable with those from D-site stations in their vicinity. This implies that effects of different site conditions would not be very large in the plain. These E-site stations are at relatively large distances ( $R_B > 30$  km), and thus the differences in type of distance measure are not so important as they are for the C-site stations ( $R_B < 15$  km). Since nearly all the C-site stations are located in the eastern margin of the plain and all the D- and E-site stations are located at the center and western side of the plain, as shown in Figure 14, the differences relative to the distance  $R_B$  could be masked easily by different site conditions.

The horizontal axes of Figure 19 represent the distance from the station to the rupture plane of the causative fault ( $r_{rup}$ ) (we used this measure of horizontal distance because that is what was used in the Abrahamson and Silva GMPEs). It seems that the largest ground motions were recorded at about 30 km away from the boundary of the plain, not at the east margin of the plain. To better show the attenuation of surface waves within the plain, we plot the observed PGAs, PGVs, and PSVs at 3 sec, 4 sec and 5 sec vs. distance to the boundary ( $R_B$ ) of the WCP in Figure 20. The large difference between Figure 19 and 20 is that they use different “distances” in plotting. In Figure 20 we only use data from 40 stations just opposite the epicenter, so that the EW and NS components should be dominated by Rayleigh and Love waves, respectively. These stations are located in the quadrangle marked in Figure 14. There is a very clear trend that the horizontal PSVs at 3 sec, 4 sec and 5 sec firstly increase with the distance  $R_B$  within about 30 km, then gradually decay with the increment of the distance. This is particularly true for the PSVs of the horizontal (EW and NS) components.

To confirm the unusual attenuation further, we plot the spatial distributions of the PSVs (EW component) at periods from 3 to 14 sec for both aftershock 1803 (Figure 21a) and aftershock 2352 (Figure 21b). In these plots the spectral amplitudes at each station have been normalized by the maximum spectral amplitude for all stations used in the plot; the normalizing spectral amplitude is given in the plot for each period. While bearing in mind the smoothing done in constructing the contours, as well as the nonuniform distribution of stations (in particular, the sparse distribution to the

east of the Chelungpu fault), it is clear that the strongest responses are in the center of the plain. The locations of the maximum amplitudes shift somewhat with period and with event.

In Figure 20, we can see that the PGA (high-frequency information) decays significantly with the increments of the distance to the boundary, while the PGV (middle-frequency information) decays very slowly. The PSVs (3-5 sec, low-frequency information) firstly increase with the increment of  $R_B$  and then decay very slowly. It seems the attenuation also depends on the period of motions. To look at the attenuation of ground motions in a large period band (1–10 sec), we plot 5%-damped PSVs (EW component) from six stations (three groups: TCU122 and CHY024,  $R_B = 9$  km; CHY026 and CHY002,  $R_B = 30$  km; CHY094 and CHY082,  $R_B = 40$  km) in Figure 22. The locations of these stations are marked in Figure 3, which are generally along the direction of seismic wave propagation. It is clear that short and short-middle period PSVs ( $< 3$  sec) decay with the increment of  $R_B$ , which are produced mostly by body waves and high-frequency surface waves. This is consistent with our present attenuation equations. However, the distance dependence of long-period ( $\geq 3$  sec) PSV is much more complex. The nearest stations TCU122 and CHY024 recorded the smallest PSVs, whereas the center stations CHY026 and CHY002 recorded the largest PSVs.

## Discussion and Conclusions

We have studied strong surface waves that were produced by an earthquake close to the western Taiwan coastal plain (WCP). The late-arriving, large-amplitude, long-period surface waves carry most of the ground motions at periods longer than 2.0 sec. The observed motions (PGVs, PSVs at 3, 4, and 5 sec) in the coastal plain are much higher than standard predictions based on general strong-motion data sets (mostly body-wave data). They are also much larger than the predictions developed by Joyner (2000) based on surface-wave data from the Los Angeles basin. The results from this work have potentially important implications for assessing long-period seismic hazards in this region for future earthquakes. Surface waves are dominant motions at periods larger than 2.0 sec. Structures whose periods are long enough to be influenced by these long-period waves are rare in the plain. Thus there are few damage reports relevant to the long-period surface waves in this region. Owing

to the rapid economic development in this region, several major communication and transportation systems have been built in recent years, and more large structures will be built in the near future. It is clear that these long-period ground motions carried by surface waves need to be taken into account for structures with periods roughly around 2 sec or larger, as well as for structures with short elastic periods which might be exceeded at about 2 sec after the structure is weakened by first part of strong motions governed by body waves.

One interesting observation from this study is that the strongest responses of long-period ground motions are in the center of the plain, about 30 km away from the boundary. The eastern boundary of the plain is very regular, extending in north-south direction. Other sides of the sediment plain are open. Hence the “**focus**” effect from boundaries of the sediment plain would be very slight. To our knowledge, there are no unusual shallow (e.g., depth < 1.5 km) subsurface structures under the center of the plain that will affect the propagation of the surface waves, although there are several such structures away from the central part of the WCP. These include the Taichung piggyback basin, about 50 km away from the center of the plain, and the Peikang basement high, about 30 km away from the center (Figure 1). The Peikang basement high lies beneath about 1.5 km of surface sediments. The localized basin and region of basement topography should not affect surface-wave propagation in the central part of the WCP.

After the Hyogo-ken Nambu earthquake of 17 January, 1985, researchers from different institutions unanimously found that heavily damaged buildings and collapsed residential houses were concentrated in a narrow zone (called the “damage belt”) oriented WSW-ENE across the city of Kobe (Kawase, 1996). The damage belt extends along the strike direction of the Rokko geological fault, but lies about 1 km away from the fault. To understand the cause of the damage belt, Kawase (1996) did numerical simulation studies. He concluded that the amplification in the ground motions 1 km away from the basin edge is caused by the coincidental collision of the direct *S*-waves with basin Rayleigh waves generated at the basin edge and radiated horizontally into the basin. It is possible that the interaction between the direct *S*-waves and the surface waves amplify short- or middle-period (e.g., < 1 sec) local ground motions; however, it would have a very slight contribution on long-period ground motions (e.g.,  $\geq 2$  sec) because long-period *S*-waves are very weak when compared with the

same period surface waves. Furthermore, the interference of the *S*-waves and surface waves would mostly happen within a short distance of the boundary. Based on studies relative to velocity structure around this region (e.g., Chen *et al.*, 2001; Satoh *et al.*, 2001), we can assume that the travel distance of the direct *S*-waves in the WCP (from the bottom to surface, the depth of the plain is about 2 km) is about 3 km, and the average travel velocity (*S*-wave velocities of sediments) in the plain is 1.5 km/sec. Accordingly, the average duration that the direct *S*-waves travel in the plain is about 2 sec (from bottom to surface). The average surface wave group velocity is about 1 km/sec (see Figure 13). Assuming the direct *S*-waves and the body waves that would be converted into surface waves at the margin of the plain enter into the plain at same time, then the place that the direct *S*-waves and surface waves could interact with each other would be within about 2 km to the boundary. This assumption is reasonable for a small or middle event (e.g.,  $M < 6.5$ ), since the duration of earthquake radiation is very short. Accordingly, we believe that the interaction of the direct *S*-waves and surface waves is not the reason for the localization of the strongest motions in the center of the coastal plain, which is about 30 km away from the boundary.

One observation from the spatial distribution of PSVs shown in Figure 21 gives us a clue to explaining the unusual attenuation of the surface waves. In Figure 21a, the “**cores**” (focus pattern of the largest PSVs) of PSV-maps for the different periods are not in the same place of the plain. It seems that the location of the “**core**” depends on the speed of the wave propagation (long-period surface waves travel faster than short-period surface waves). If the strongest ground motions were caused by the amplification of specific surface sediments or subsurface structures, or by the focus of basin structures, they would be at same place. We conjecture that multi-pathing surface waves (generated in the boundary area) overlap each other along their propagation path and add constructively. As a result, the ground motions get stronger and stronger. Beyond a certain distance to the boundary, no new surface waves were generated. In turn, the ground motions tend to decay along their propagation path. Since the long-period surface waves travel faster than the short-period surface waves, they would overlap each other in a larger distance range. The mechanism of the conversion from body waves to surface waves at edges of sedimentary waveguides is not well understood. A common agreement is that this conversion would happen at “**margins**” of basins or plains. However, there are no clear

results about how wide the “margin” needs to be. Based on the work of this study, we think that the width of the “margin” could be very considerable. For the case studied in this article, the “margin” could be as wide as 30 km.

## Acknowledgments

We thank Dr. Robert B. Herrmann for supplying his program of calculating group velocity and review the manuscript carefully, Dr. Neil D. Selby and Dr. Jeffry L. Stevens for their thoughtful suggestions on calculating the backazimuth of Rayleigh waves, Dr. Chris Mortgat and two BSSA anonymous reviewers for their careful corrections and thoughtful suggestions. We also thank NCREE and CWB for providing the  $P - S$  logging data, Dr. Walt Silva for interpreting data, and Dr. Brian Chiou for supplying his inferred  $\bar{V}_s(30)$  data. This work was supported in part by the National Science Foundation under Grant GEO-0302967.

## References

- Abrahamson, N. A., and W. J. Silva (1997). Empirical response spectral attenuation relations for shallow crustal earthquakes, *Seism. Res. Lett.* **68**, 94-127.
- Baker, G. E., and J. L. Stevens (2004). Backazimuth estimation reliability using surface wave polarization, *Geophys. Res. Lett.*, **31**, L09611, doi:10.1029/2004GL019510.
- Bonner, J., and E. T. Herrin (1999). Surface wave studies of the Sierra Madre Occidental of northern Mexico, *Bull. Seism. Soc. Am.* **89**, 1323-1337.
- Boore, D. M. (2005). On pads and filters: Processing strong-motion data, *Bull. Seism. Soc. Am.* **95**, 745-750.
- Boore, D. M. (2003). Phase derivatives and simulation of strong ground motions, *Bull. Seism. Soc. Am.* **93**, 1132-1143.
- Boore, D. M. (2001a). Effect of baseline correction on displacement and response spectra for several recordings of the 1999 Chi-Chi, Taiwan, earthquake, *Bull. Seism. Soc. Am.* **91**, 1199-1211.



Boore, D. M. (2001b). Comparisons of ground motions from the 1999 Chi-Chi earthquake with empirical predictions largely based on data from California, *Bull. Seism. Soc. Am.* **91**, 1212-1217.

Boore, D. M. (1999a). Basin waves on a seafloor recording of the 1999 Upland, California, earthquake: implications for ground motions from a larger earthquake, *Bull. Seism. Soc. Am.* **89**, 317-324.

Boore, D. M. (1999b). Effect of baseline corrections on response spectra for two recordings of the 1999 Chi-Chi, Taiwan, earthquake, *U.S. Geol. Surv. Open-File Rept.* 99-545.

Boore, D. M. and W. B. Joyner (1997). Site amplifications for generic rock sites, *Bull. Seism. Soc. Am.* **87**, 327-341.

Boore, D. M., K. L. Larner, and K. Aki (1971). Comparison of two independent methods for the solution of wave-scattering problems: Response of a sedimentary basin to vertically incident *SH* waves, *J. Geophys. Res.* **76**, 558-569.

Boore, D. M., V. M. Graizer, J. G. Tinsley, and A. F. Shakal (2004). A study of possible ground-motion amplification at the Coyote Lake dam, California, *Bull. Seism. Soc. Am.* **94**, 1327-1342.

Boore, D. M., W. B. Joyner, and T. E. Fumal (1997). Equations for estimating horizontal response spectra and peak acceleration from western north American earthquakes: A summary of recent work, *Seism. Res. Lett.* **68**, 128-153.

Building Seismic Safety Council (BSSC) (1995). 1994 Edition NEHRP Recommended Provisions for Seismic Regulations for New Buildings, FEMA 222A/223A, developed for the Federal Emergency Management Agency, Washington, D. C.

Building Seismic Safety Council (BSSC) (1998). 1997 Edition NEHRP Recommended Provisions for Seismic Regulations for New Buildings, FEMA 302/303, developed for the Federal Emergency Management Agency, Washington, D. C.

Building Seismic Safety Council (BSSC) (2001). NEHRP recommended provisions for seismic regulations for new buildings and other structures, 2000 Edition, Part 1: Provisions, prepared by the Building Seismic Safety Council for the Federal Emergency Management Agency (Report FEMA 368), Washington, D. C.

Campbell, K. W. (2001). Appendix to Strong motion attenuation relations: commentary and

discussion of selected relations, in IASPEI Handbook of Earthquake and Engineering Seismology, W. H. K. Lee (Editor) Academic Press, San Diego, California.

Campbell, K. W. (2000). Erratum to Empirical near-source attenuation relationships for horizontal and vertical components of peak ground acceleration, peak ground velocity, and pseudo-absolute acceleration response spectra by Kenneth W. Campbell, *Seism. Res. Lett.* **71**, 353-355.

Campbell, K. W. (1997). Empirical near-source attenuation relationships for horizontal and vertical components of peak ground acceleration, peak ground velocity, and pseudo-absolute acceleration response spectra, *Seism. Res. Lett.* **68**, 154-179.

Campbell, K. W. and Y. Bozorgnia (2003). Updated near-source ground-motion (attenuation) relations for the horizontal and vertical components of peak ground acceleration and acceleration response spectra, *Bull. Seism. Soc. Am.* **93**, 314-331.

Chael, E. P. (1997). An automated Rayleigh-wave detection algorithm, *Bull. Seism. Soc. Am.* **87**, 157-163.

Chang, S. S. L. (1971). Subsurface geologic study of the Taichung basin, Taiwan, *Pet. Geol. Taiwan* **8**, 21-45.

Chen, C.-H., W.-H. Wang, and T.-L. Teng (2001). 3D velocity structure around the source area of the 1999 Chi-Chi, Taiwan, Earthquake: before and after the mainshock, *Bull. Seism. Soc. Am.* **91**, 1013-1027.

Chi, W.-C., and D. Dreger (2004). Crustal Deformation in Taiwan: Results from Finite Source inversions of six  $M_w > 5.8$  Chi-Chi aftershocks, *Geophys. Res. Lett.* **109**, B07305, doi:10.1029/2003JB002606.

Cornou, C., P.-Y. Bard, and M. Dietrich (2003). Contribution of dense array analysis to the identification and quantification of basin-edge-induced waves, part II: application to Grenoble basin (French Alps), *Bull. Seism. Soc. Am.* **93**, 2624-2648.

Davis, D., J. Suppe, and F. A. Dehlen (1983). Mechanisms of fold-and-thrust belts and accretionary wedges, *J. Geophys. Res.* **88**, 1153-1172.

Dobry, R., R. D. Borchardt, C. B. Crouse, I. M. Idriss, W. B. Joyner, G. R. Martin, M. S. Power, E. E. Rinne, and R. B. Seed (2000). New site coefficients and site classification system used in recent

building seismic code provisions, *Earthquake Spectra* 16, 41-67.

Dziewonski, A., S. Bloch, and M. Landisman (1969). A technique for the analysis of transient seismic signals, *Bull. Seism. Soc. Am.* **59**, 427-444.

Field, E. H., and the SCES Phase III Working Group (2000). Accounting for site effects in probabilistic seismic hazard analyses of southern California: overview of the SCEC phase III report, *Bull. Seism. Soc. Am.* **90**, S1-S31.

Field, E. H. (1996). Spectral amplification in a sediment-filled valley exhibiting clear basin-edge-induced waves, *Bull. Seism. Soc. Am.* **86**, 991-1005.

Frankel, A., S. Hough, P. Friberg, and R. Busby (1991). Observations of Loma Prieta aftershocks from a dense array in Sunnyvale, California, *Bull. Seism. Soc. Am.* **91**, 1900-1922.

Frankel, A., D. Carver, E. Cranswick, T. Bice, R. Sell, and S. Hanson (2001). Observations of basin ground motions from a dense seismic array in San Jose, California, *Bull. Seism. Soc. Am.* **91**, 1-12.

Goforth, T. T., and E. T. Herrin (1979). Phase-matched filters: application to the study of Love waves. *Bull. Seism. Soc. Am.* **69**, 27-44.

Graves, R. W., A. Pitarka, and P. G. Somerville (1998). Ground-motion amplification in the Santa Monica area: effects of shallow basin-edge structure, *Bull. Seism. Soc. Am.* **88**, 1224-1242.

Graves, R. W. and D. J. Wald (2004). Observed and simulated ground motions in the San Bernardino basin region for the Hector Mine, California, earthquake, *Bull. Seism. Soc. Am.* **94**, 131-146.

Hanks, T. C. (1975). Strong ground motion of the San Fernando, California, earthquake: ground displacements, *Bull. Seism. Soc. Am.* **65**, 193-225.

Hartzell, S., D. Carver, R. A. Williams, A. Harmsen, and A. Zerva (2003). Site response, shallow shear-wave velocity, and wave propagation at the San Jose, California, dense seismic array, *Bull. Seism. Soc. Am.* **93**, 443-464.

Herrmann, R. B. (2002). Computer programs in seismology, version 3.25. Department of Earth and Atmospheric sciences, Saint Louis University (<http://www.eas.slu.edu>).

Hsiao, P. T. (1971). Seismic study of the area between the coastal plain and the foothills, Yunlin,

Taiwan, *Pet. Geol. Taiwan*, 8, 249-263.

Iida, M., and H. Kawase (2004). A comprehensive interpretation of strong motions in the Mexican volcanic belt, *Bull. Seism. Soc. Am.* **94**, 598-618.

Joyner, W. B. (2000). Strong motion from surface waves in deep sedimentary basins, *Bull. Seism. Soc. Am.* **90**, S95-S112.

Kawase, H. (1996). The cause of the damage belt in Kobe: “ the basin-edge effect”, constructive interference of the direct *S*-wave with the basin-induced diffracted/Rayleigh waves, *Seism. Res. Lett.* **67**, 25-34.

Koch, K., and B. W. Stump (1996). The Constraints for Upper Mantle Shear Wave Models of the Basin and Range from Surface Wave Inversion, *Bull. Seism. Soc. Am.* **86**, 1591-1607.

Komatitsch, D., Q. Liu, J. Tromp, P. Süß, C. Stidham, and J. H. Shaw (2004). Simulations of ground motion in the Los Angeles Basin based upon the Spectral-Element Method, *Bull. Seism. Soc. Am.* **94**, 187–206.

Lee, W. H. K., T. C. Shin, and C. F. Wu (2001). CWB Free-Field Strong-Motion Data from Three Major Aftershocks of the 1999 Chi-Chi Earthquake: Processed Acceleration Data Files on CD-ROM, CWB Strong-Motion Data Series CD-002, Seismological Observation Center, Central Weather Bureau, Taipei, Taiwan, August 28, 2001.

Liu, H.-L., and T. H. Heaton (1984). Array analysis of the ground velocities and accelerations from the 1971 San Fernando, California, earthquake, *Bull. Seism. Soc. Am.* **74**, 1951-1968.

Lu, C.-Y., H. Chu, J. Lee, Y. Chan, K. Chang, and F. Mouthereau (2002). The 1999 Chi-Chi Taiwan earthquake and basement impact thrust kinematics, *Western Pacific Earth Sciences*, Vol.2, No.2, 181-190.

Rovelli, A., L. Scognamiglio, F. Marra, and A. Caserta (2003). Edge-diffracted 1-sec surface waves observed in a small-size intramountain basin (Colfiorito, Central Italy), *Bull. Seism. Soc. Am.* **91**, 1851-1866.

Sadigh, K., C.-Y. Chang, J. A. Egan, F. Makdisi, and R. R. Youngs (1997). Attenuation relationships for shallow crustal earthquakes based on California strong motion data, *Seism. Res. Lett.* **68**, 180-189.

Satoh, T., H. Kawase, T. Iwata, S. Higashi, T. Sato, K. Irikura, and H.-C. Huang (2001). *S*-wave velocity structure of the Taichung Basin, Taiwan, estimated from array and single-station records of microtremors, *Bull. Seism. Soc. Am.* **91**, 1267-1282.

Selby, N. D. (2001). Association of Rayleigh waves using backazimuth measurements: application to Test Ban verification, *Bull. Seism. Soc. Am.* **91**, 580-593.

Shin, T.-C., and T. Teng (2001). An overview of the 1999 Chi-Chi, Taiwan, Earthquake, *Bull. Seism. Soc. Am.* **91**, 895-913.

Stach, L.-W. (1958). Subsurface exploration and geology of the coastal plain region of Western Taiwan, *Proc. Geol. Soc. China*, 1, 55-96.

Suppe, J. (1981). Mechanics of mountain building and metamorphism in Taiwan, *Mem. Geol. Soc. China*, 4, 67-89.

Tang, J. H. (1977). Late miocene erosional unconformity on the subsurface Peikang High beneath the Chiayi-Yunlin, Coastal Plain, Taiwan, *Mem. Geol. Soc. China*, 2, 155-167.

Tanimoto, T., and L. Rivera (2005). Prograde Rayleigh Wave Particle Motion, *Geophys. J. Int.*, **162**, 399-405.

Teng, L. S. (1990) Geotectonic evolution of late Cenozoic arc-continent collision in Taiwan, *Tectonophysics*, 183, 57-77.

Vidale, J. E., and D. V. Helmberger (1988). Elastic finite-difference modeling of the 1971 San Fernando, California earthquake, *Bull. Seism. Soc. Am.* **78**, 122-141.

Wang, G.-Q., D. M. Boore, H. Igel, and X.-Y. Zhou (2004). Comparisons of ground motions from five aftershocks of the 1999 Chi-Chi, Taiwan earthquake with empirical predictions largely based on data from California, *Bull. Seism. Soc. Am.* **94**, 2198-2212.

Wang, G.-Q, D.M. Boore, H. Igel, and X.-Y. Zhou (2003). Some Observations on colocated and Closely Spaced Strong Ground-Motion Records of the 1999 Chi-Chi, Taiwan, Earthquake, *Bull. Seism. Soc. Am.* **93**, 674-693.

Wang, G.-Q, X.-Y. Zhou, P.-Z. Zhang, and H. Igel (2002). Characteristics of amplitude and duration for near fault strong ground motion from the 1999 Chi-Chi, Taiwan, Earthquake, *Soil Dyn. Earthq. Eng.* **22**, 73-96.

Wang, G.-Q, X.-Y. Zhou, Z.-J. Ma, and P.-Z. Zhang (2001). Data files from “A preliminary study on the randomness of response spectra of the 1999 Chi-Chi, Taiwan, Earthquake”, *Bull. Seism. Soc. Am.* **91**, 1388-1389.

Wells, D. L., and K. J. Coppersmith (1994). New empirical relationships among magnitude, rupture length, rupture width, rupture area, and surface displacement, *Bull. Seism. Soc. Am.* **84**, 974-1002.

Wen, S., and C.-H. Chen (2004). 3-D velocity structure beneath the Chia-Nan area, Taiwan, *TAO* (Terrestrial, Atmospheric and Oceanic Sciences), Vol. 15, No.2, 239-259.

Applied Geophysical Science Laboratories  
North Carolina A & T State University  
1020 E. Wendover Ave.  
Greensboro, 27411  
gwang@ncat.edu, gtang@ncat.edu  
(G.-Q.W., G.-Q.T., G.V.N.B., C.R.J., Q.-L.L.)

U.S. Geological Survey, MS 977  
345 Middlefield Road  
Menlo Park, California 94025  
boore@usgs.gov  
(D.M.B.)

College of Architectural and Civil Engineering  
Beijing University of Technology  
Beijing, 100022 China  
zhouxy@bjut.edu.cn  
(X.-Y.Z.)

Table 1: Main Source Parameters of the 1999 Chi-Chi Mainshock and its Five Aftershocks Studied in This Article\* (from Wang *et al.* 2004)

Event	Origin time (UTC: m/d/y, h/m/s)	Epicenter Long. (E)	(degree) Lat. (N)	Depth (km)	$M_L$	$M_w$	Strike (Deg.)	Dip (Deg.)	Rake (Deg.)
Main	09/20/99, 17:47:00	120.82	23.85	11	7.3	7.6	20	30	85
1803	09/20/99, 18:03:41	120.86	23.81	8	6.6	6.2	0	10	80
0014	09/22/99, 00:14:40	121.08	23.81	10	6.8	6.2	165	70	100
2352	09/25/99, 23:52:49	121.01	23.87	16	6.8	6.3	5	30	100
1757	09/20/99, 17:57:15	121.01	23.94	8	6.4	5.8	200	41	78
2146	09/20/99, 21:46:37	120.82	23.60	18	6.6	6.2	330	89	15

\* The five aftershocks are named according to their origin times. Parameters of the 1999 Chi-Chi mainshock are from (Shin and Teng, 2001). The origin time and  $M_L$  of aftershocks are from Lee *et al.* (2001); other parameters are from Chi and Dreger (2004).



# List of Figures

- 1     Topographic map showing the epicenters of the 1999 Chi-Chi mainshock, aftershock 1803 and other four aftershocks mentioned in this article. The large gray star represents the epicenter of the Chi-Chi mainshock (at UTC 17:47, 20 September, 1999; **M** 7.6). The dark stars represent the epicenters of event 1803 (at UTC 18:03, 20 September, 1999; **M** 6.2) and other four aftershocks named as 1757, 2146, 2352, and 0014. Source information of these five aftershocks is listed in Table 1. The small triangles represent 250 strong ground-motion stations from which records triggered by event 1803 are available from Lee *et al.* (2001). Measured  $\overline{V}_s(30)$  data are available for 144 stations (dark triangles) among these 250 stations from PEER NGA database (<http://peer.berkeley.edu/nga/>). The heavy curve on the left side of epicenter area is the Chelungpu-Chukou fault, which is regarded as the eastern boundary of the western Taiwan coastal plain (WCP) in this study. The gray curves at the left side of the Chelungpu-Chukou fault represent the Changhua and Chiuchunkun faults. The heavy line across the plain from west to east indicates the location of the geologic profile shown in Figure 2. . . . . 40
  
- 2     A sketch showing the geologic cross section (after Teng, 1990) of the Western Coastal Plain. The location of this profile is marked in Figure 1. . . . . 41
  
- 3     Map showing (a) acceleration and (b) displacement time series (east-west component, from 15 to 65 sec of original records) observed in the Western Coastal Plain of the Taiwan Island during aftershock 1803. Note that these traces are not adjusted for travel time differences. The heavy curve extending from north to south represents the Chelungpu-Chukou fault. . . 42

- 4 Acceleration, velocity and displacement time series of the radial direction from station CHY025 induced by the Chi-Chi mainshock and five aftershocks. The location of station CHY025 is shown in Figure 3. These records are aligned with *P*-wave arrivals. Significant late-arriving, long-period surface waves can be observed from traces of events 1803 and 2352; obvious surface waves can also be observed from the traces of events 0014 and 2146. 43
- 5 An example showing that surface waves and body waves separate very well in both the time domain and the frequency domain. (a) Three-component (radial, transverse, and vertical) acceleration time series and Fourier amplitude spectra for event 1803 recorded at station CHY025. The surface waves start at about 30 sec, then overlap with the body waves (mostly *S*-waves) from 30 to 34 sec. (b) The 5%-damped pseudovelocity (PSV) response spectra for the whole trace (0—70 sec), the body wave segment (0—30 sec), and the surface wave segment (30—70 sec). The PSV curve of the whole trace overlaps with the curve of the body within 0.5 sec, while it overlaps with the curve of the surface wave after about 0.5 sec. 44
- 6 The particle motion plots (hodograms) of body wave and Rayleigh wave at station CHY025 during event 1803. (a) The acceleration time series of horizontal (radial direction) and vertical components. (b) The displacement time series of horizontal (radial direction) and vertical components. The motions before 30-sec are body waves; the motions after 30-sec are dominated by Rayleigh waves. (c) The hodogram of acceleration from 20 to 60 sec. (d) The hodogram of displacement from 20 to 60 sec. Subfigures at the right sides of (c) and (d) are the hodograms at six segments (0–20 sec, 20–27 sec, 27–30 sec, 30–38 sec, 38–50 sec, 50–60 sec) of ground motions. The gray circle refers to the start of particle motion, and the dark circle refers to the end of particle motion. . . . . 45

- 7 Rayleigh waves for stations near the eastern edge of the plain and in the middle of the WCP. The top subfigure shows the horizontal displacement traces (EW component) from four stations — TCU129 ( $R_B = 1.5$  km), TCU076 ( $R_B = 2.5$  km), TCU122 ( $R_B = 9$  km) and CHY026 ( $R_B = 30$  km) — which are dominated by the Rayleigh waves. Locations of these stations are plotted in Figure 3. The subfigures b–e show the Rayleigh waves at periods 3 sec, 5 sec and 7 sec extracted from the original traces of TCU129, TCU076, TCU122, and CHY026 using a Gaussian filter. The subfigure f shows multi-pathing wave trains (phases with period of 2 sec) included in the surface waves. We do not do any alignments for traces from different stations. Note that different scales are used in ordinate axes. . . . . 46
- 8 Acceleration time series (vertical component) and Fourier spectra from three stations TCU129, TCU076, and TCU079 recorded during event 1803. The Fourier amplitudes have been smoothed slightly. Stations TCU129 and TCU076 are inside the plain, while station TCU079 is outside the plain (see Figure 3). Three traces are aligned with  $P$ -arrivals. . . . 47
- 9 An illustration of the process used to calculate the backazimuth of Rayleigh wave propagation. The location of station TCU118 is marked in Figure 3. (a) Comparisons of  $S_{z\bar{r}}/S_{zz}$  and  $S_{z\bar{r}}/\sqrt{S_{zz}S_{\bar{r}\bar{r}}}$  as a function of the trial backazimuth; (b) comparisons of the vertical, Hilbert transformed radial, and radial displacements; (c) the bandpass filtered displacement traces of vertical, north-south (NS), and east-west (EW) components. An acausal, fourth-order Butterworth filter (0.15–3.3 Hz) is used. (d) The displacement traces of vertical, radial, and transverse components. To get the radial and transverse components, the original NS and EW traces are rotated  $117^\circ$  (measured clockwise from north), which is the backazimuth of the Rayleigh wave propagation obtained from Equation (2). . . . . 48

10	A map showing directions of the Rayleigh wave propagations in the WCP. The heavy curve extending from north to south represents the Chelungpu-Chukou fault. The gray rectangle represents the horizontal projection of the fault rupture. The width (8 km) and length (15 km) of the fault rupture are estimated according to the empirical relationship between earthquake magnitude and fault parameters developed by Wells and Coppersmith (1994). .	49
11	A map showing propagations of the Rayleigh waves (vertical direction) from station CHY024 ( $R_B = 9$ km), through CHY002 ( $R_B = 28$ km) to CHY027 ( $R_B = 42$ km). Locations of these stations are plotted in Figure 3, which are roughly in the radial direction of surface wave propagations. The Rayleigh phases with periods from 2 sec to 8 sec are extracted from original displacement traces (top subfigure) with a Gaussian filter. All traces are aligned according to absolute UTC time. . . . .	50
12	An illustration of output from the Multiple Filter Analysis (MFA) program “do_mft” developed by Robert B. Herrmann (2002). (a) Group velocity dispersion of the horizontal-component Rayleigh wave calculated from the record observed at station CHY026 during event 1803. The different black symbols represent the group velocities of the Rayleigh wave with different modes. The contours represent the spectra amplitudes. The gray-scale represents the signal strength from black (smallest) to white (largest). (b) Same as (a) but the group velocity dispersion as revised by the program Phase Matched Filtering (PMF). .	51
13	Average group-velocity dispersion curves of the Love and Rayleigh waves obtained after applying the MFA and PMF programs for records from 16 stations marked in Figure 10. $\sigma$ represents the standard deviation. . . . .	52

14	Maps showing $\overline{V}_s(30)$ and site classifications in the western Taiwan coastal plain. Records from 90 stations are available in the plain from Lee <i>et al.</i> (2001). (a) Map showing $\overline{V}_s(30)$ data at these stations ( <a href="http://peer.berkeley.edu/nga">http://peer.berkeley.edu/nga</a> ). Dark circles represent measured $\overline{V}_s(30)$ , and gray triangles represent inferred $\overline{V}_s(30)$ . (b) Map showing site classes based on $\overline{V}_s(30)$ (the NEHRP standards). Totally, there are 40 C-site ( $360 < \overline{V}_s(30) < 760$ m/sec), 46 D-site ( $180 < \overline{V}_s(30) < 360$ m/sec), and 4 E-site ( $\overline{V}_s(30) < 180$ m/sec) stations. The quadrangle indicates the locations of records used in plotting Figure 20. . . . .	53
15	Ratios of energy carried by surface waves ( $E_{Love}$ , horizontal $E_{Rayleigh}$ , and vertical $E_{Rayleigh}$ ) to the total energy ( $E_{Total}$ ) carried by the surface waves from the 90 stations (40 C-sites, 46 D-sites, and 4 E-sites) in the plain (see Figure 14). The horizontal lines represent the average value and the average plus/minus one standard deviation. . . . .	54
16	Maps showing spatial distributions of the horizontal Peak Ground Acceleration (PGA), Peak Ground Velocity (PGV), and Peak Ground Displacement (PGD) observed during aftershock 1803. The large star represents the location of the epicenter. The small triangles represent the stations whose records are used in plotting the contour maps. The horizontal PGA, PGV, and PGD are the geometric means of the NS and EW values. The PGA, PGV, and PGD values are extracted from corrected records. See text for more information about data processing. . . . .	55
17	(a) Horizontal peak ground velocities (PGVs) observed in the western Taiwan coastal plain during event 1803 vs. predicted PGVs that would be generated by an event like event 1803 at generic soil sites according to the ground-motion prediction equations of Campbell (1997, 2000). These observed PGVs are from all stations in the plain (Figure 14). (b) Same figure for the Chi-Chi mainshock. Note, the predictions of the Campbell (1997, 2000) are for generic soil sites. . . . .	56

18	Observed 5%-damped pseudoacceleration (PSA) response spectra at 3 sec and 4 sec vs. the predictions from the equations of Campbell and Bozorgnia (2003). The predictions are for the motions at firm-soil sites produced by a $M_w$ 6.2, thrust-faulting event. The observed PSVs are from all stations in the plain (Figure 14). The left column is for the horizontal component, and the right column is for the vertical component. The horizontal PSAs are the geometrical means of the NS and EW values. . . . .	57
19	Observed 5%-damped pseudovelocity (PSV) response spectra at periods 3 sec, 4 sec, and 5 sec vs. predictions from Joyner (2000), based on data from the Los Angeles basin. The light lines show the Abrahamson and Silva relationship (1997) for a $M$ 6.2 event (reverse faulting) at generic soil sites. The gray heavy lines show the 5%-damped pseudovelocity response values given by Joyner's predictions (2000) using the Abrahamson and Silva (1997) ground-motion prediction equations. These symbols represent all observed PSVs in the plain (see Figure 14). The abscissa represents distance to the fault rupture plane ( $r_{rup}$ ) for these observations and predictions of Abrahamson and Silva (1997), and $R_E + R_B$ for predictions of Joyner (2000). $R_E$ is the distance from the epicenter to the Chelungpu-Chukou fault. $R_B$ is the distance from the station to the boundary. The east-west (EW) and north-south (NS) motions correspond approximately to the perpendicular and parallel components of surface wave propagation in Joyner's predictions. . . . .	58
20	Attenuation of observed ground motions (PGA, PGV, PSV at 3 sec, 4 sec, and 5 sec) in the western Taiwan coastal plain. The main difference between this figure and previous figure (Figure 19) is that the distance to the boundary ( $R_B$ ), rather than the distance to the source rupture ( $r_{rup}$ ) is used in plotting this figure. Furthermore, data only from 40 stations just opposite to the epicenter are used. The locations of these stations are in the quadrangle marked in Figure 14. To highlight the changes of observed motion with the increment of $R_B$ , we draw the gray strips manually. . . . .	59

21	Maps showing spatial distributions of pseudovelocity (PSV) response spectra at periods from 3 sec to 14 sec calculated from the observed strong ground motion records (EW component) during aftershocks 1803 and 2352. The large stars represent the location of epicenters. The small triangles represent stations whose records are used in plotting the contour maps. . . . .	60
22	5%-damped pseudovelocity (PSV) response spectra from six stations (Three groups: [1] TCU122 and CHY024, $R_B = 9$ km; [2] CHY026 and CHY002, $R_B = 30$ km; [3] CHY094 and CHY082, $R_B = 40$ km). The locations of these stations are marked in Figure 3. . . .	61

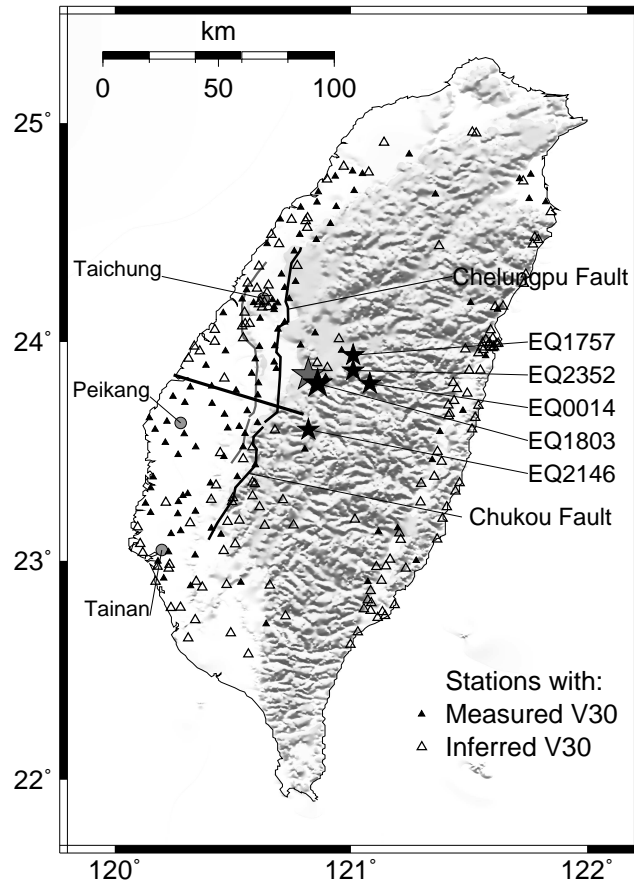


Figure 1: Topographic map showing the epicenters of the 1999 Chi-Chi mainshock, aftershock 1803 and other four aftershocks mentioned in this article. The large gray star represents the epicenter of the Chi-Chi mainshock (at UTC 17:47, 20 September, 1999;  $M$  7.6). The dark stars represent the epicenters of event 1803 (at UTC 18:03, 20 September, 1999;  $M$  6.2) and other four aftershocks named as 1757, 2146, 2352, and 0014. Source information of these five aftershocks is listed in Table 1. The small triangles represent 250 strong ground-motion stations from which records triggered by event 1803 are available from Lee *et al.* (2001). Measured  $\bar{V}_s(30)$  data are available for 144 stations (dark triangles) among these 250 stations from PEER NGA database (<http://peer.berkeley.edu/nga/>). The heavy curve on the left side of epicenter area is the Chelungpu-Chukou fault, which is regarded as the eastern boundary of the western Taiwan coastal plain (WCP) in this study. The gray curves at the left side of the Chelungpu-Chukou fault represent the Changhua and Chiuchunkun faults. The heavy line across the plain from west to east indicates the location of the geologic profile shown in Figure 2.



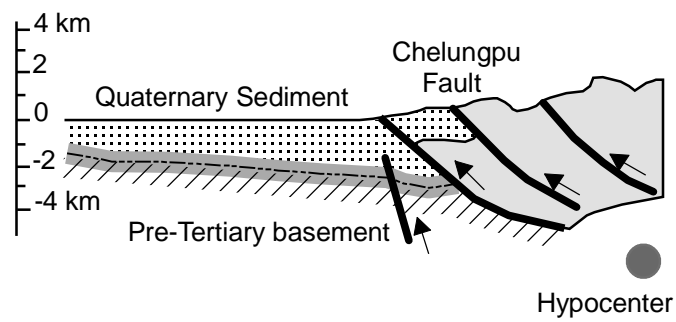


Figure 2: A sketch showing the geologic cross section (after Teng, 1990) of the Western Coastal Plain. The location of this profile is marked in Figure 1.

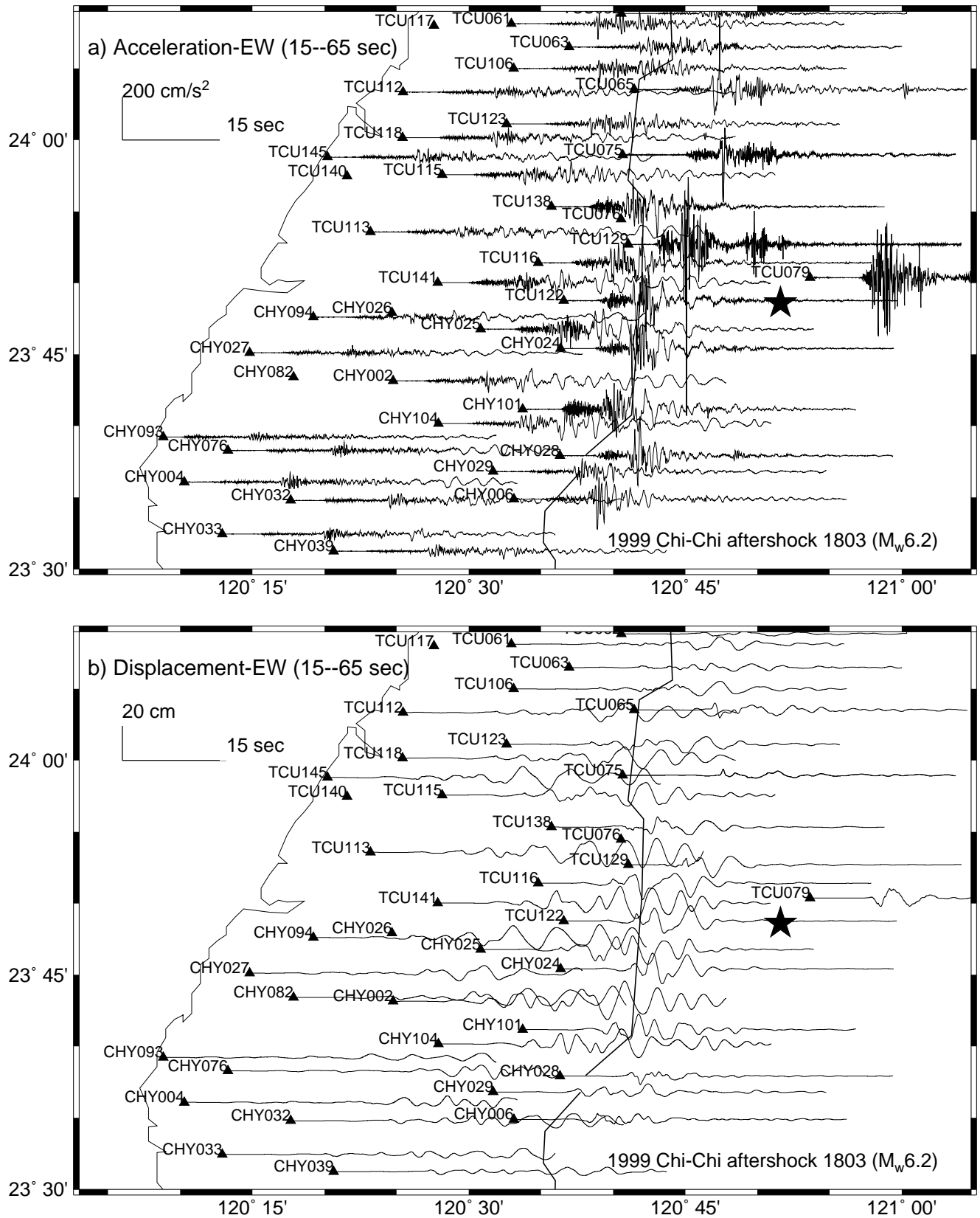


Figure 3: Map showing (a) acceleration and (b) displacement time series (east-west component, from 15 to 65 sec of each record) observed in the Western Coastal Plain of the Taiwan Island during aftershock 1803. Note that these traces are not adjusted for travel time differences. The heavy curve extending from north to south represents the Chelungpu-Chukou fault.

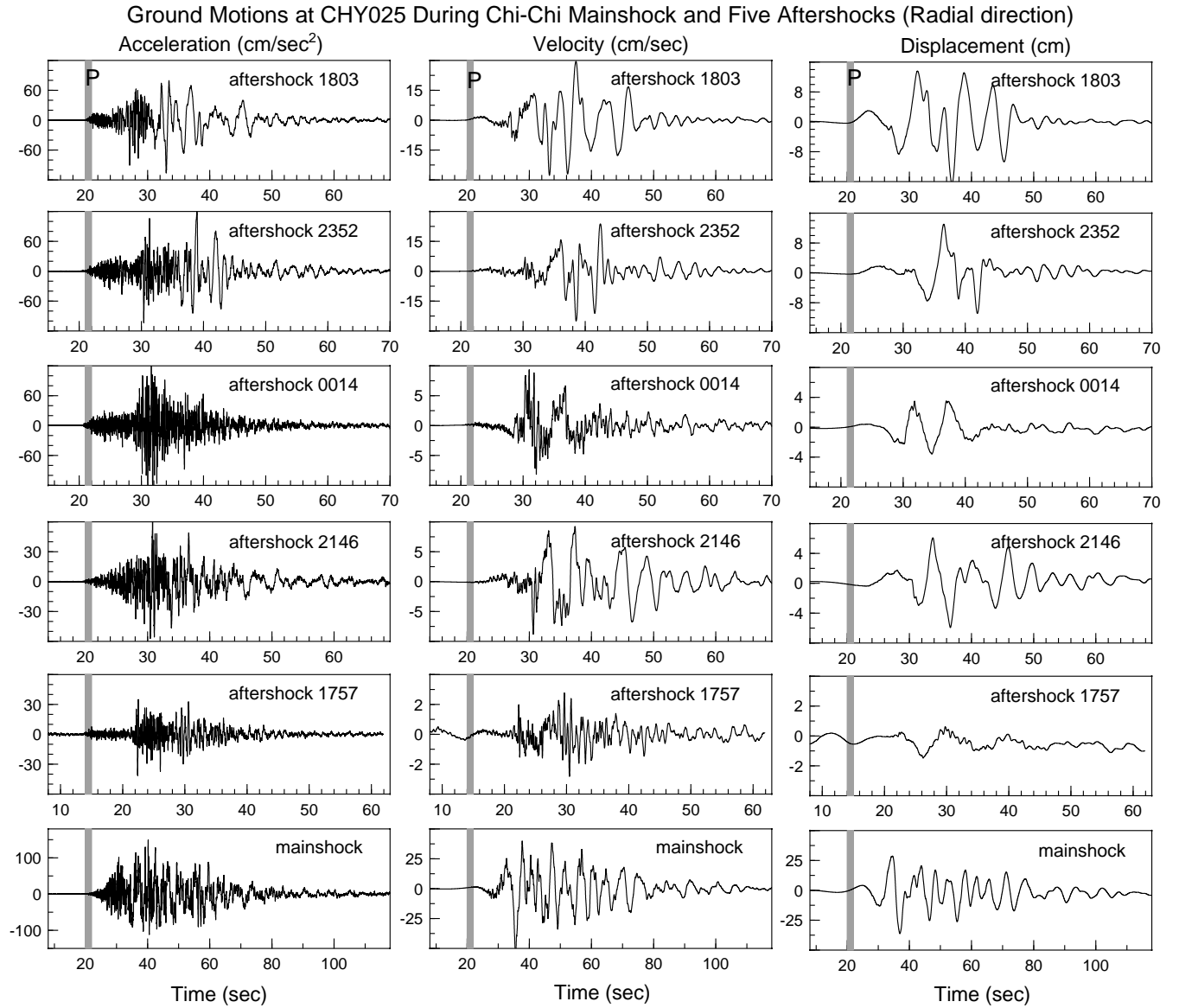
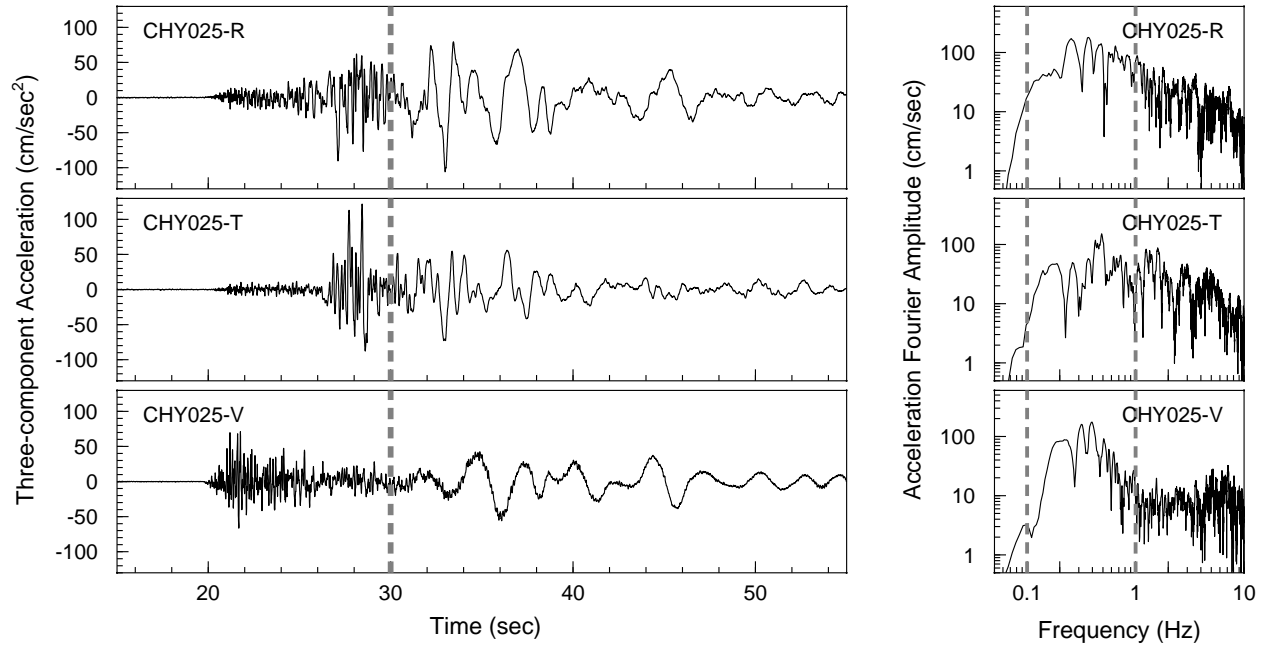
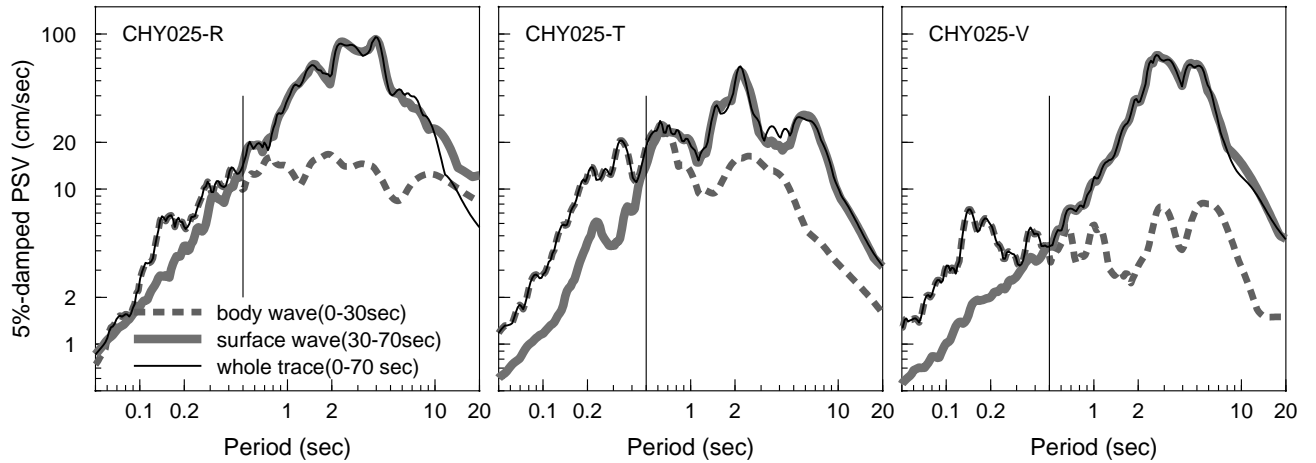


Figure 4: Acceleration, velocity and displacement time series of the radial directions from station CHY025 induced by the Chi-Chi mainshock and five aftershocks. The location of station CHY025 is shown in Figure 3. These records are aligned with *P*-wave arrivals. Significant late-arriving, long-period surface waves can be observed from traces of events 1803 and 2352; obvious surface waves can also be observed from the traces of events 0014 and 2146.



(a)



(b)

Figure 5: An example showing that surface waves and body waves separate very well in both the time domain and the frequency domain. (a) Three-component (radial, transverse, and vertical) acceleration time series and Fourier amplitude spectra for event 1803 recorded at station CHY025. The surface waves start at about 30 sec, then overlap with the body waves (mostly *S*-waves) from 30 to 34 sec. (b) The 5%-damped pseudovelocity (PSV) response spectra for the whole trace (0—70 sec), the body wave segment (0—30 sec), and the surface wave segment (30—70 sec).

Rayleigh Wave from CHY025, the Chi-Chi aftershock 1803 ( $M_w 6.2$ )

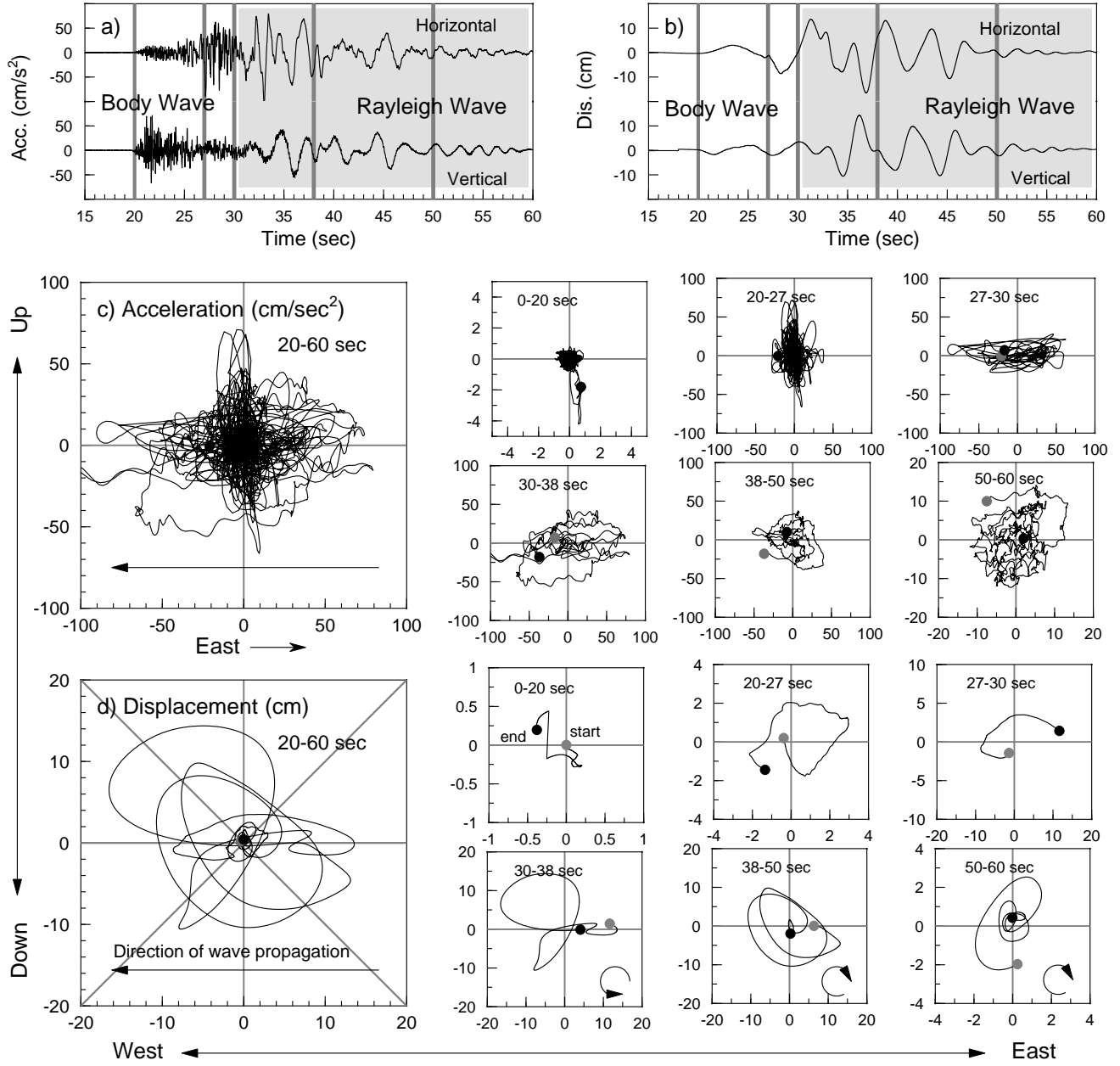


Figure 6: The particle motion plots (hodograms) of body wave and Rayleigh wave at station CHY025 during event 1803. (a) The acceleration time series of horizontal (radial direction) and vertical components. (b) The displacement time series of horizontal (radial direction) and vertical components. The motions before 30-sec are body waves; the motions after 30-sec are dominated by Rayleigh waves. (c) The hodogram of acceleration from 20 to 60 sec. (d) The hodogram of displacement from 20 to 60 sec. Subfigures at the right sides of (c) and (d) are the hodograms at six segments (0–20 sec, 20–27 sec, 27–30 sec, 30–38 sec, 38–50 sec, 50–60 sec) of ground motions. The gray circle refers to the start of particle motion, and the dark circle refers to the end of particle motion.

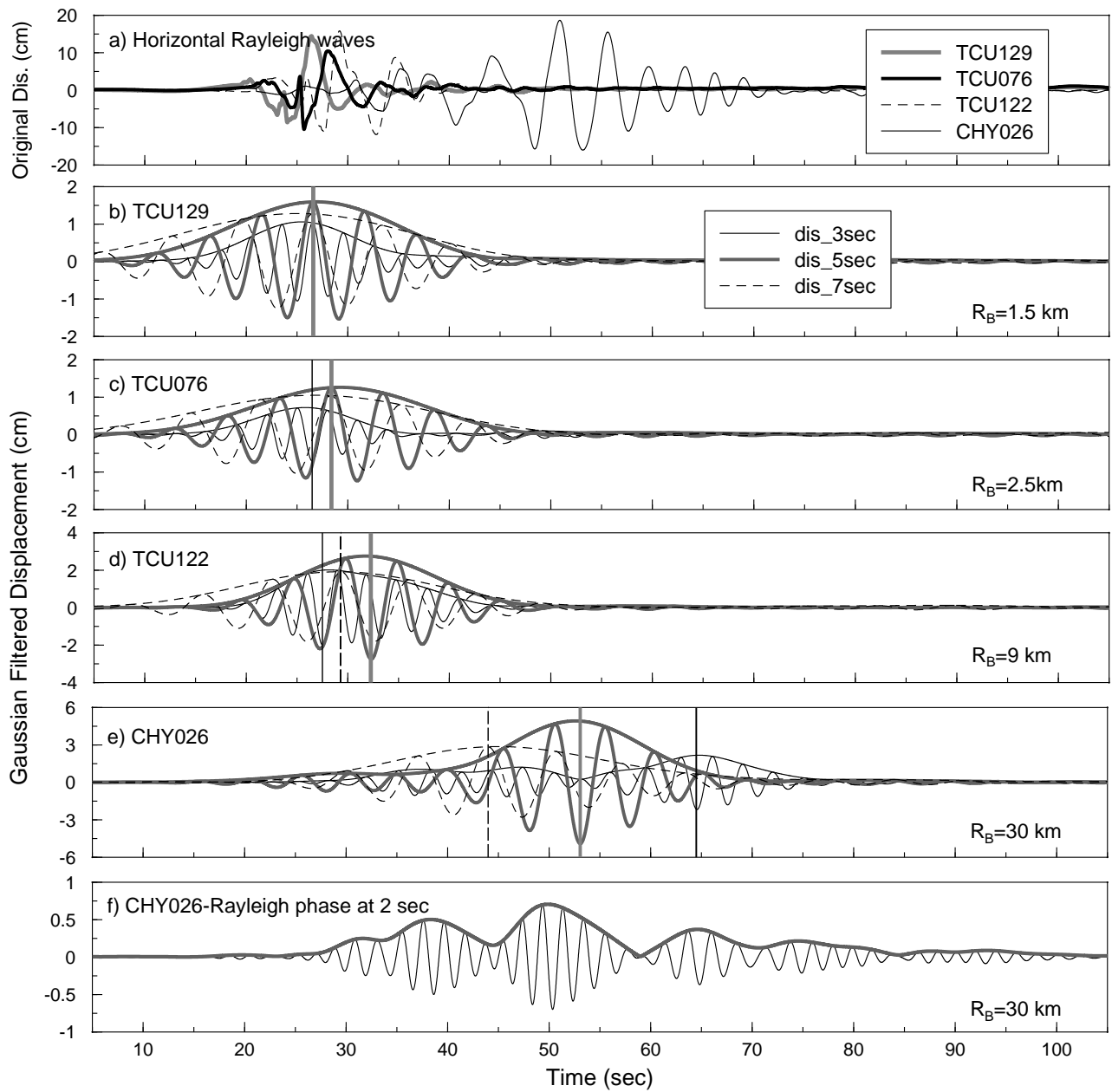


Figure 7: Rayleigh waves for stations near the eastern edge of the plain and in the middle of the WCP. The top subfigure shows the horizontal displacement traces (EW component) from four stations — TCU129 ( $R_B = 1.5$  km), TCU076 ( $R_B = 2.5$  km), TCU122 ( $R_B = 9$  km) and CHY026 ( $R_B = 30$  km) — which are dominated by the Rayleigh waves. Locations of these stations are plotted in Figure 3. The subfigures b–e show the Rayleigh waves at periods 3 sec, 5 sec and 7 sec extracted from the original traces of TCU129, TCU076, TCU122, and CHY026 using a Gaussian filter. The subfigure f shows multi-pathing wave trains (phases with period of 2 sec) included in the surface waves. We do not do any alignments for traces from different stations. Note that different scales are used in ordinate axes.

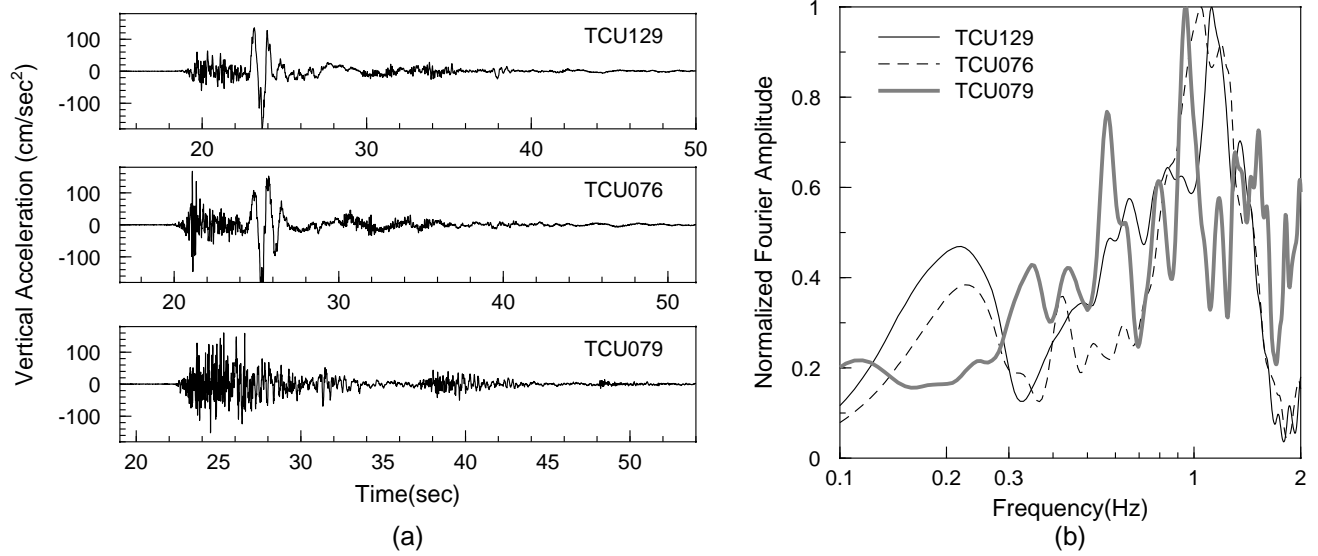


Figure 8: Acceleration time series (vertical component) and Fourier spectra from three stations TCU129, TCU076, and TCU079 recorded during event 1803. The Fourier amplitudes have been smoothed slightly. Stations TCU129 and TCU076 are inside the plain, while station TCU079 is outside the plain (see Figure 3). Three traces are aligned with *P*-arrivals.

Rayleigh and Love waves recorded at station TCU118 during the aftershock 1803

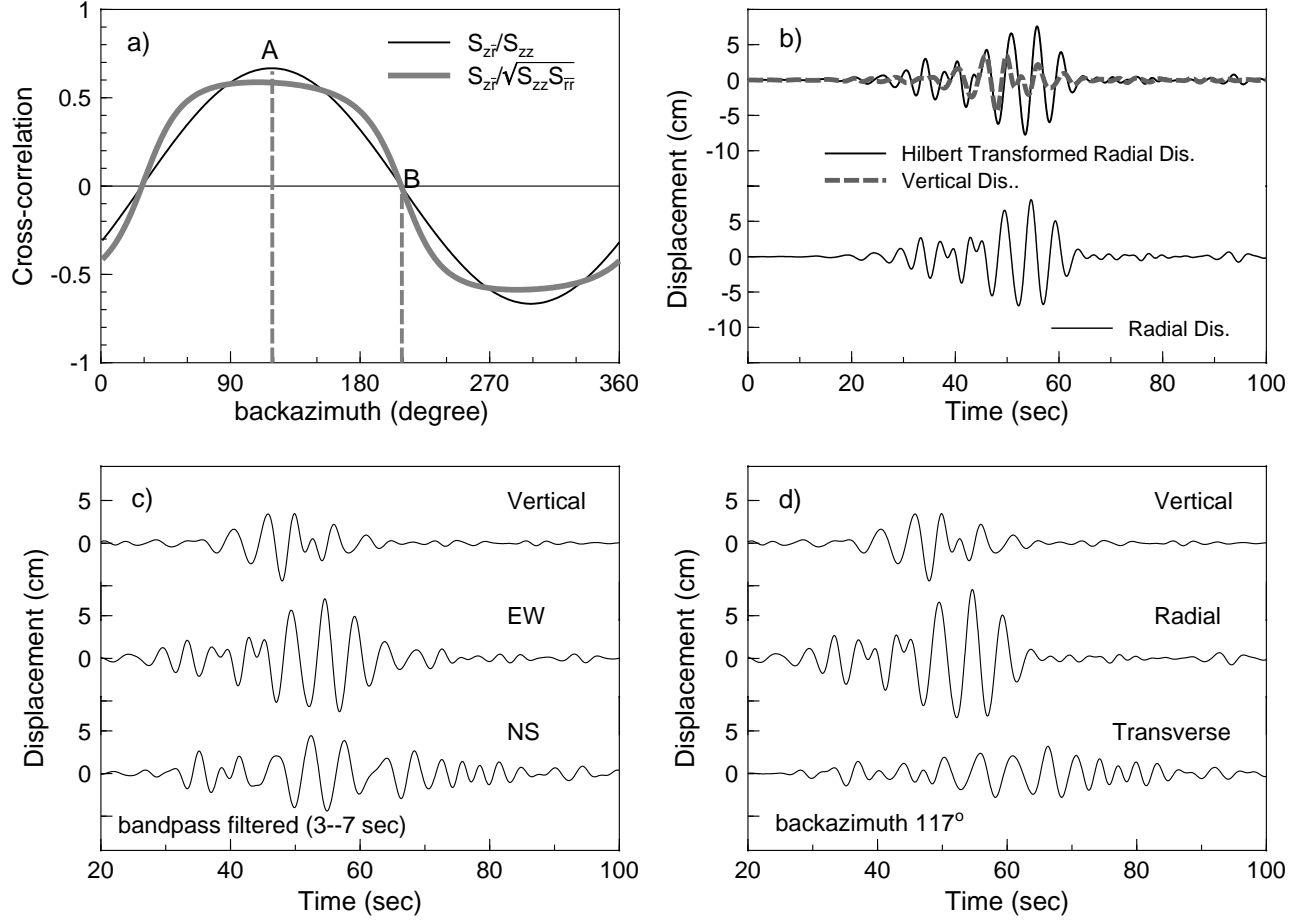


Figure 9: An illustration of the process used to calculate the backazimuth of Rayleigh wave propagation. The location of station TCU118 is marked in Figure 3. (a) Comparisons of  $S_{z\bar{r}}/S_{zz}$  and  $S_{z\bar{r}}/\sqrt{S_{zz}S_{\bar{r}\bar{r}}}$  as a function of the trial backazimuth; (b) comparisons of the vertical, Hilbert transformed radial, and radial displacements; (c) the bandpass filtered displacement traces of vertical, north-south (NS), and east-west (EW) components; (d) the displacement traces of vertical, radial, and transverse components. To get the radial and transverse components, the original NS and EW traces are rotated  $117^\circ$  (measured clockwise from north), which is the backazimuth of the Rayleigh wave propagation obtained from Equation (2).



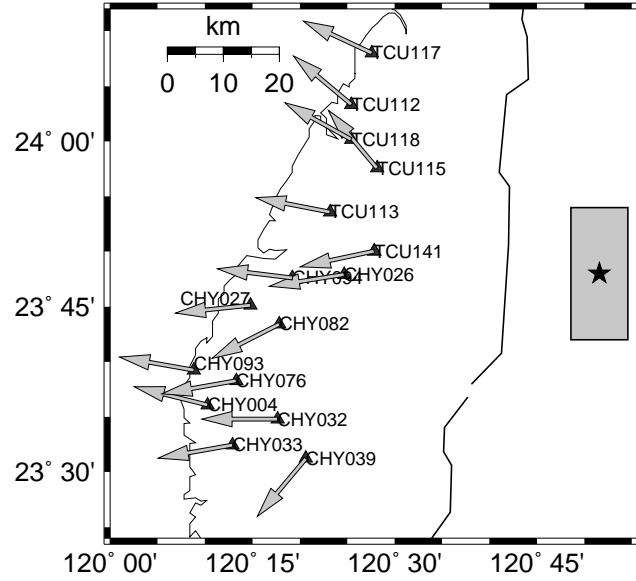


Figure 10: A map showing directions of the Rayleigh wave propagations in the WCP. The heavy curve extending from north to south represents the Chelungpu-Chukou fault. The gray rectangle represents the horizontal projection of the fault rupture. The width (8 km) and length (15 km) of the fault rupture are estimated according to the empirical relationship between earthquake magnitude and fault parameters developed by Wells and Coppersmith (1994).

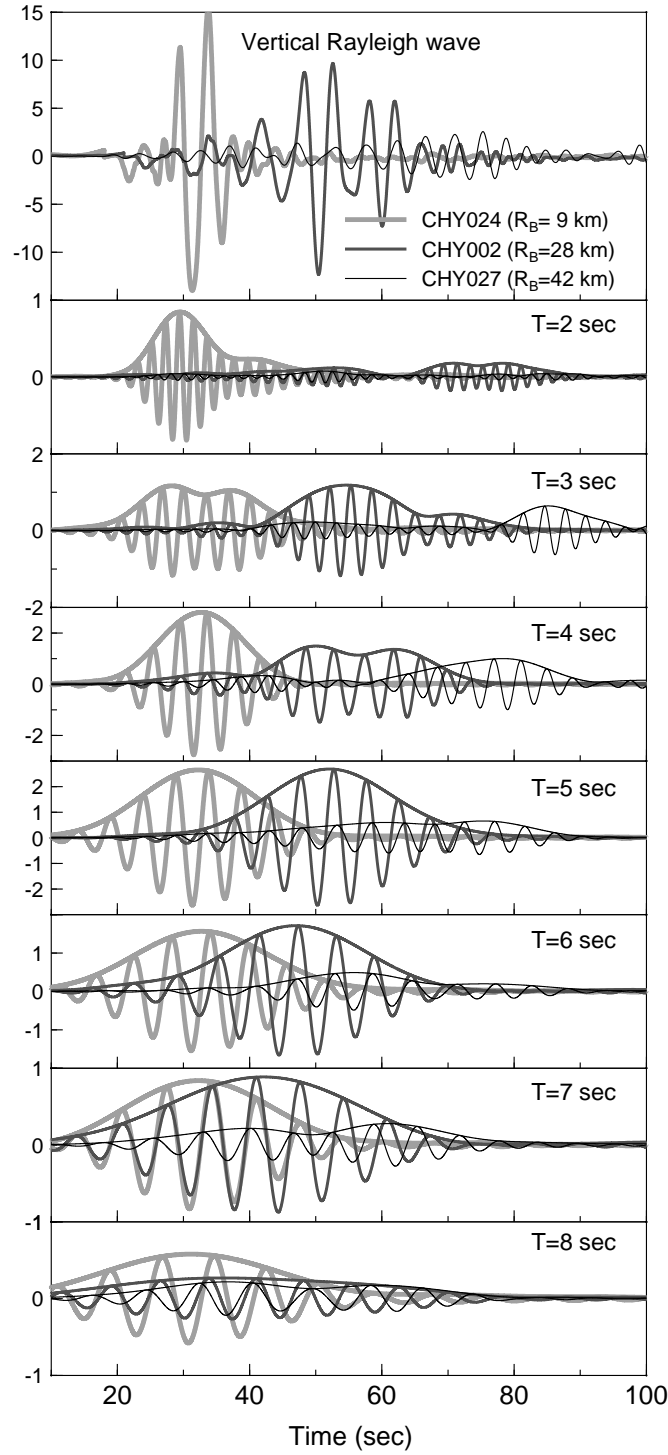
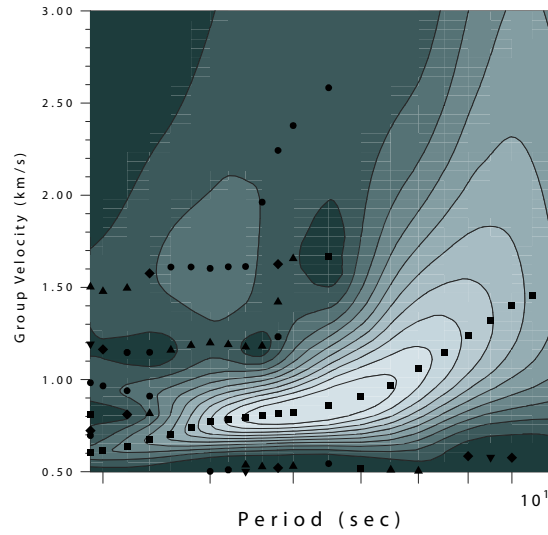
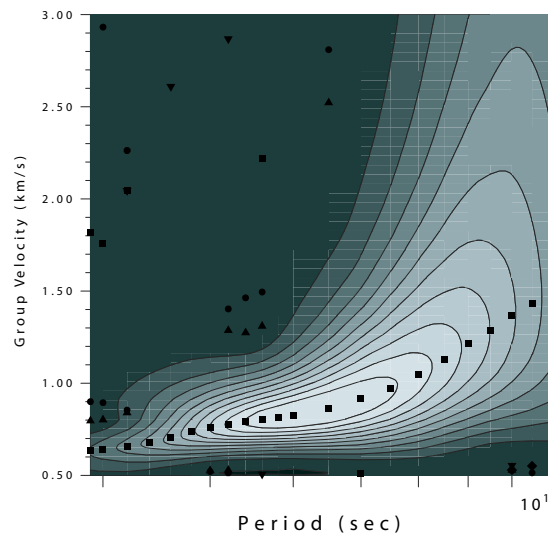


Figure 11: A map showing propagations of the Rayleigh waves (vertical direction, in cm) from station CHY024 ( $R_B = 9$  km), through CHY002 ( $R_B = 28$  km) to CHY027 ( $R_B = 42$  km). Locations of these stations are plotted in Figure 3, which are roughly on a line with the epicenter. The Rayleigh phases with periods from 2 sec to 8 sec are extracted from original displacement traces (top subfigure) with a Gaussian filter. All traces are aligned according to the absolute UTC time.



(a)



(b)

Figure 12: An illustration of output from the Multiple Filter Analysis (MFA) program “do\_mft” developed by Robert B. Herrmann (2002). (a) Group velocity dispersion of the horizontal-component Rayleigh wave calculated from the record observed at station CHY026 during event 1803. The different black symbols represent the group velocities of the Rayleigh wave with different modes. The contours represent the spectra amplitudes. The gray-scale represents the signal strength from black (the smallest) to white (the largest). (b) Same as (a) but the group velocity dispersion as revised by the program Phase Matched Filtering (PMF).

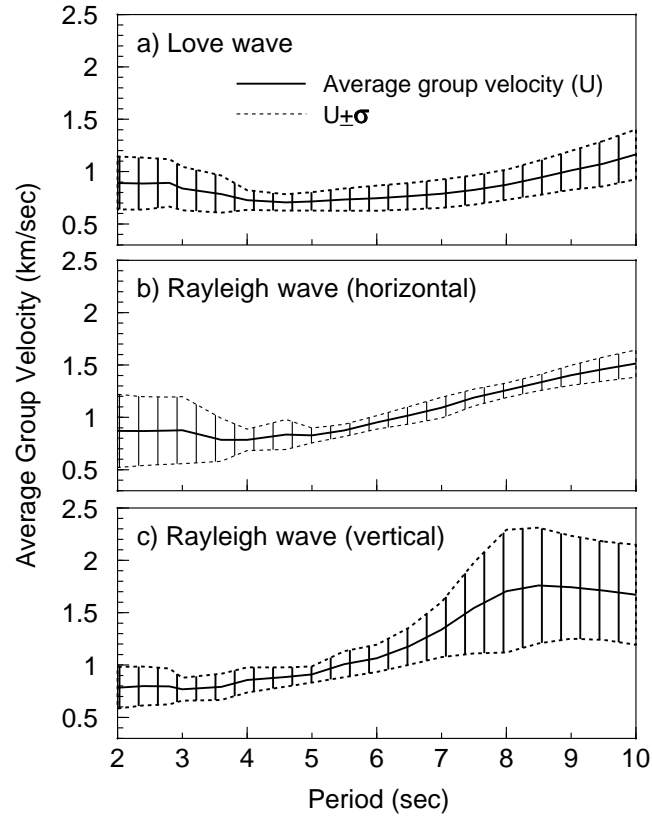


Figure 13: Average group-velocity dispersion curves of the Love and Rayleigh waves obtained after applying the MFA and PMF programs for records from 16 stations marked in Figure 10.  $\sigma$  represents the standard deviation.

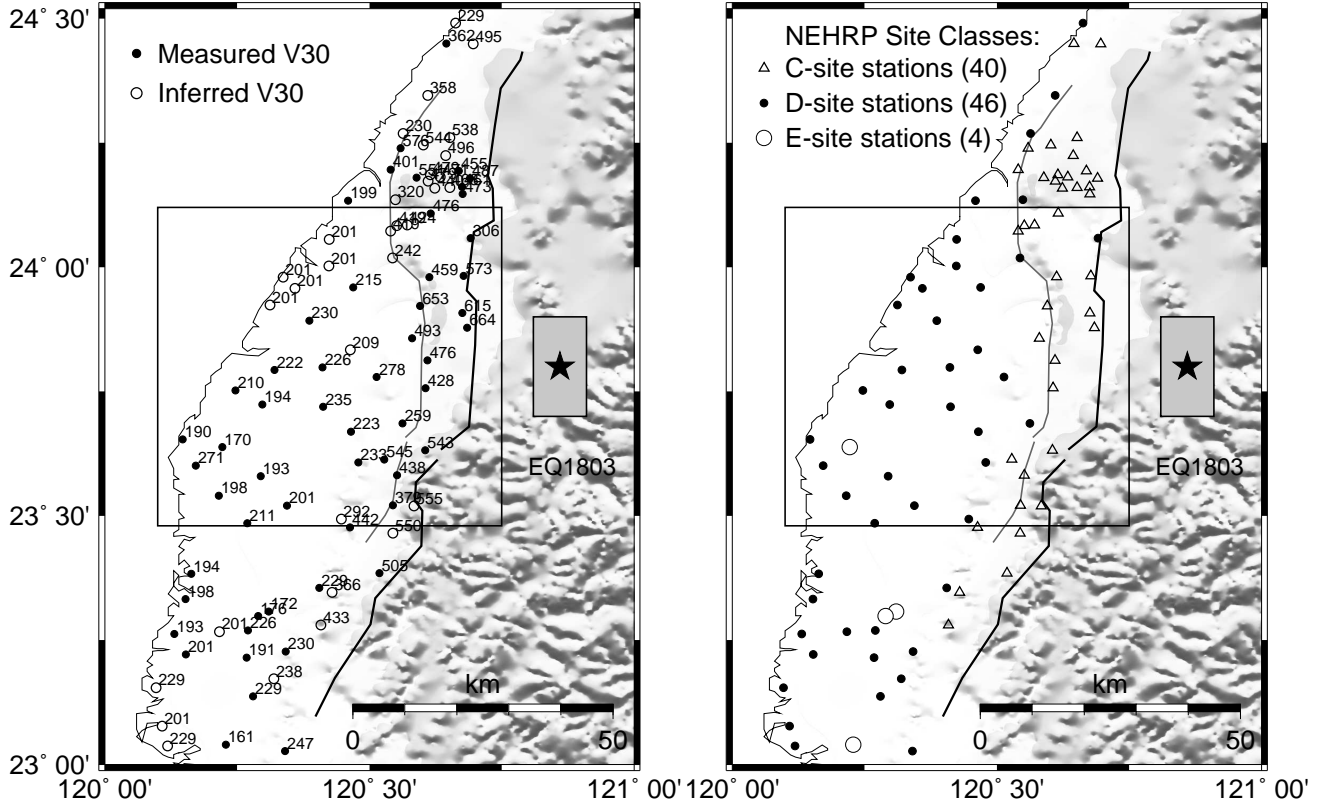


Figure 14: Maps showing  $\bar{V}_s(30)$  and site classifications in the western Taiwan coastal plain. Records from 90 stations are available in the plain from Lee *et al.* (2001). (a) Map showing  $\bar{V}_s(30)$  data at these stations (<http://peer.berkeley.edu/nga>). Dark circles represent measured  $\bar{V}_s(30)$ , and gray triangles represent inferred  $\bar{V}_s(30)$ . (b) Map showing site classes based on  $\bar{V}_s(30)$  (the NEHRP standards). Totally, there are 40 C-site ( $360 < \bar{V}_s(30) < 760$  m/sec), 46 D-site ( $180 < \bar{V}_s(30) < 360$  m/sec), and 4 E-site ( $\bar{V}_s(30) < 180$  m/sec) stations. The quadrangle indicates the locations of records used in plotting Figure 20.

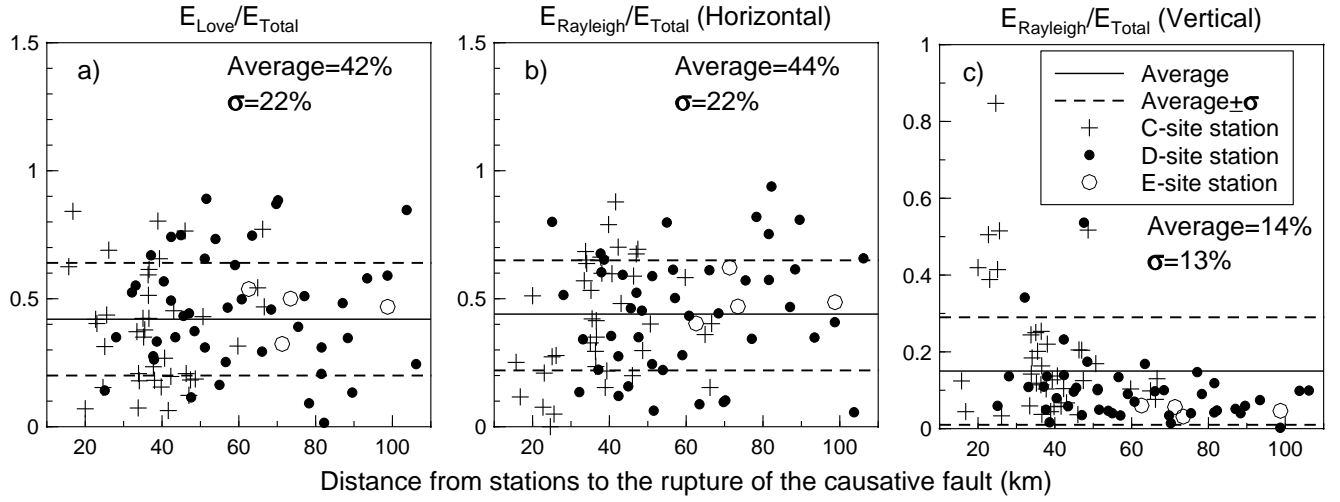


Figure 15: Ratios of energy carried by surface waves ( $E_{Love}$ , horizontal  $E_{Rayleigh}$ , and vertical  $E_{Rayleigh}$ ) to the total energy ( $E_{Total}$ ) carried by the surface waves from the 90 stations (40 C-sites, 46 D-sites, and 4 E-sites) in the plain (see Figure 14). The horizontal lines represent the average value and the average plus/minus one standard deviation.

1999 Chi-Chi, Taiwan, aftershock 1803 ( $M_w 6.2$ )

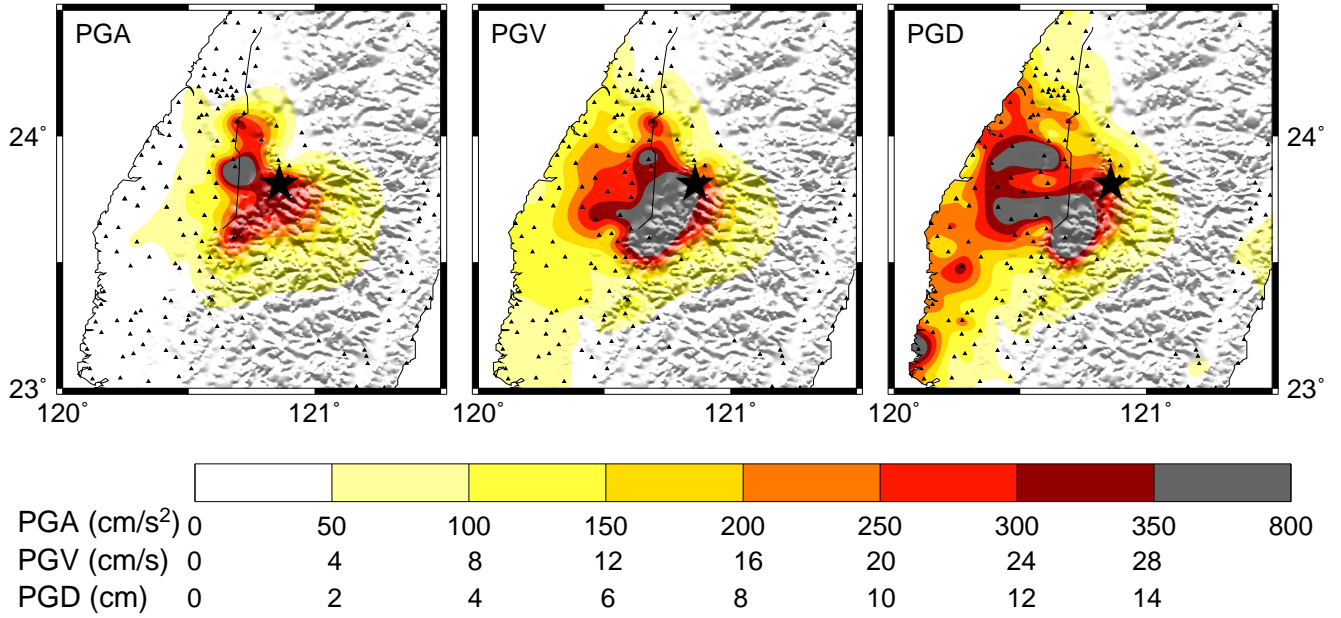


Figure 16: Maps showing spatial distributions of the horizontal Peak Ground Acceleration (PGA), Peak Ground Velocity (PGV), and Peak Ground Displacement (PGD) observed during aftershock 1803. The large star represents the location of the epicenter. The small triangles represent the stations whose records are used in plotting the contour maps. The horizontal PGA, PGV, and PGD are the geometric means of the NS and EW values. The PGA, PGV, and PGD values are extracted from corrected records. See text for more information about data processing.

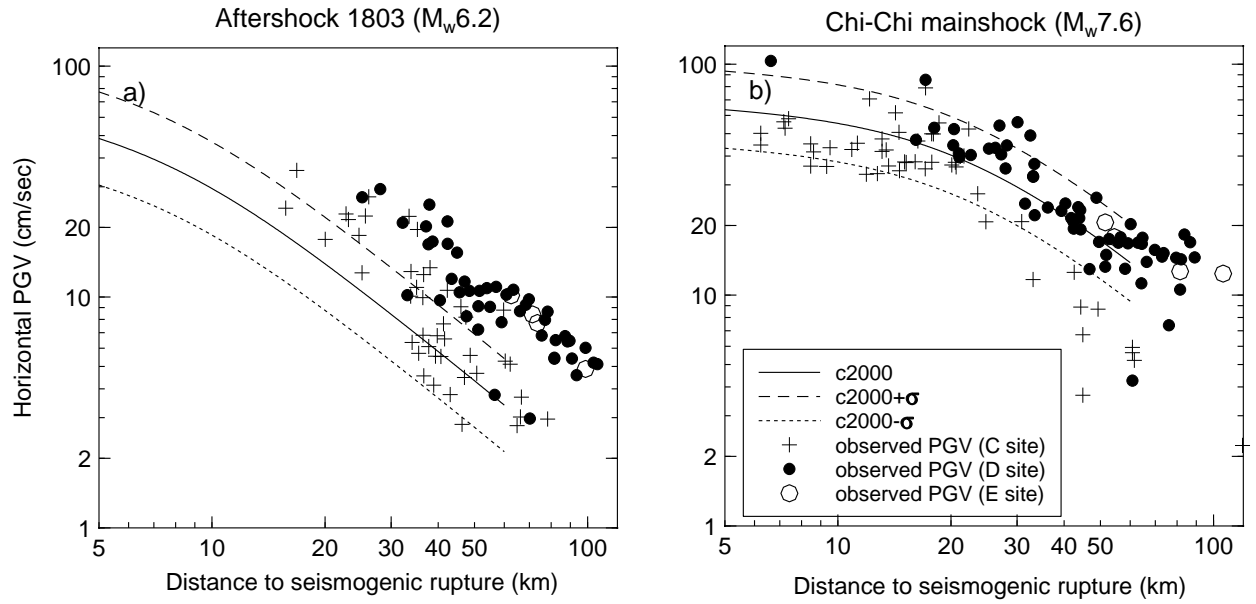


Figure 17: (a) Horizontal peak ground velocities (PGVs) observed in the western Taiwan coastal plain during event 1803 vs. predicted PGVs that would be generated by an event like event 1803 at generic soil sites according to the ground-motion prediction equations of Campbell (1997, 2000). These observed PGVs are from all stations in the plain (Figure 14). (b) Same figure for the Chi-Chi mainshock. Note that the predictions of the Campbell (1997, 2000) are for generic soil sites.



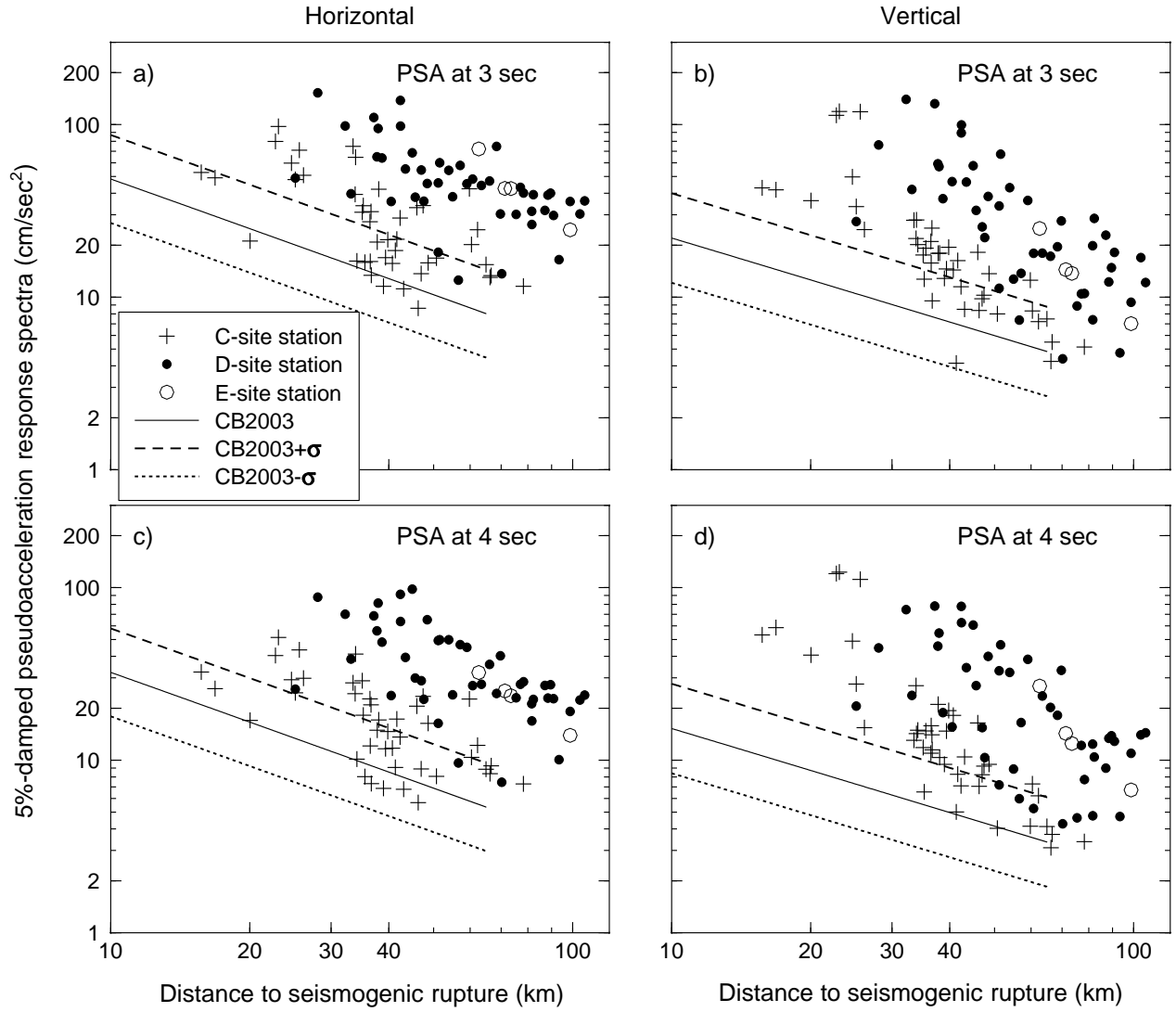


Figure 18: Observed 5%-damped pseudoacceleration (PSA) response spectra at 3 sec and 4 sec vs. the predictions from the equations of Campbell and Bozorgnia (2003). The predictions are for the motions at firm-soil sites produced by a  $M_w$  6.2, thrust-faulting event. The observed PSVs are from all stations in the plain (Figure 14). The left column is for the horizontal component, and the right column is for the vertical component. The horizontal PSAs are the geometrical means of the NS and EW values.

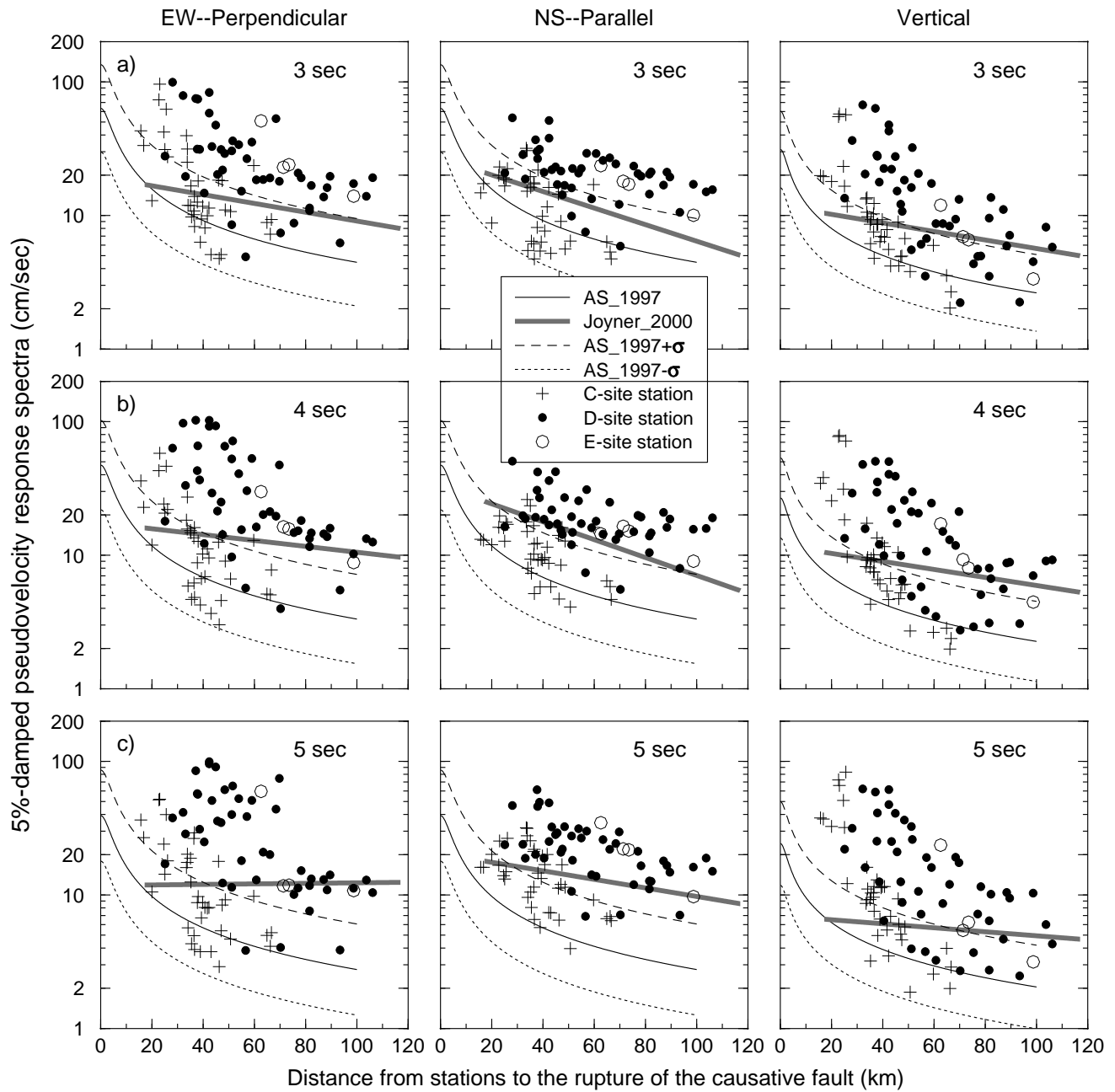


Figure 19: Observed 5%-damped pseudovelocity (PSV) response spectra at periods 3 sec, 4 sec, and 5 sec vs. predictions from Joyner (2000), based on data from the Los Angeles basin. The light lines show the Abrahamson and Silva relationship (1997) for a  $M$  6.2 event (reverse faulting) at generic soil sites. The gray heavy lines show the 5%-damped pseudovelocity response values given by Joyner's predictions (2000) using the Abrahamson and Silva (1997) ground-motion prediction equations. These symbols represent all observed PSVs in the plain (see Figure 14). The abscissa represents distance to the fault rupture plane ( $r_{rup}$ ) for these observations and predictions of Abrahamson and Silva (1997), and  $R_E + R_B$  for predictions of Joyner (2000).  $R_E$  is the distance from the epicenter to the Chelungpu-Chukou fault.  $R_B$  is the distance from the station to the boundary.<sup>58</sup> The east-west (EW) and north-south (NS) motions correspond approximately to the perpendicular and parallel components of surface wave propagation in Joyner's predictions.

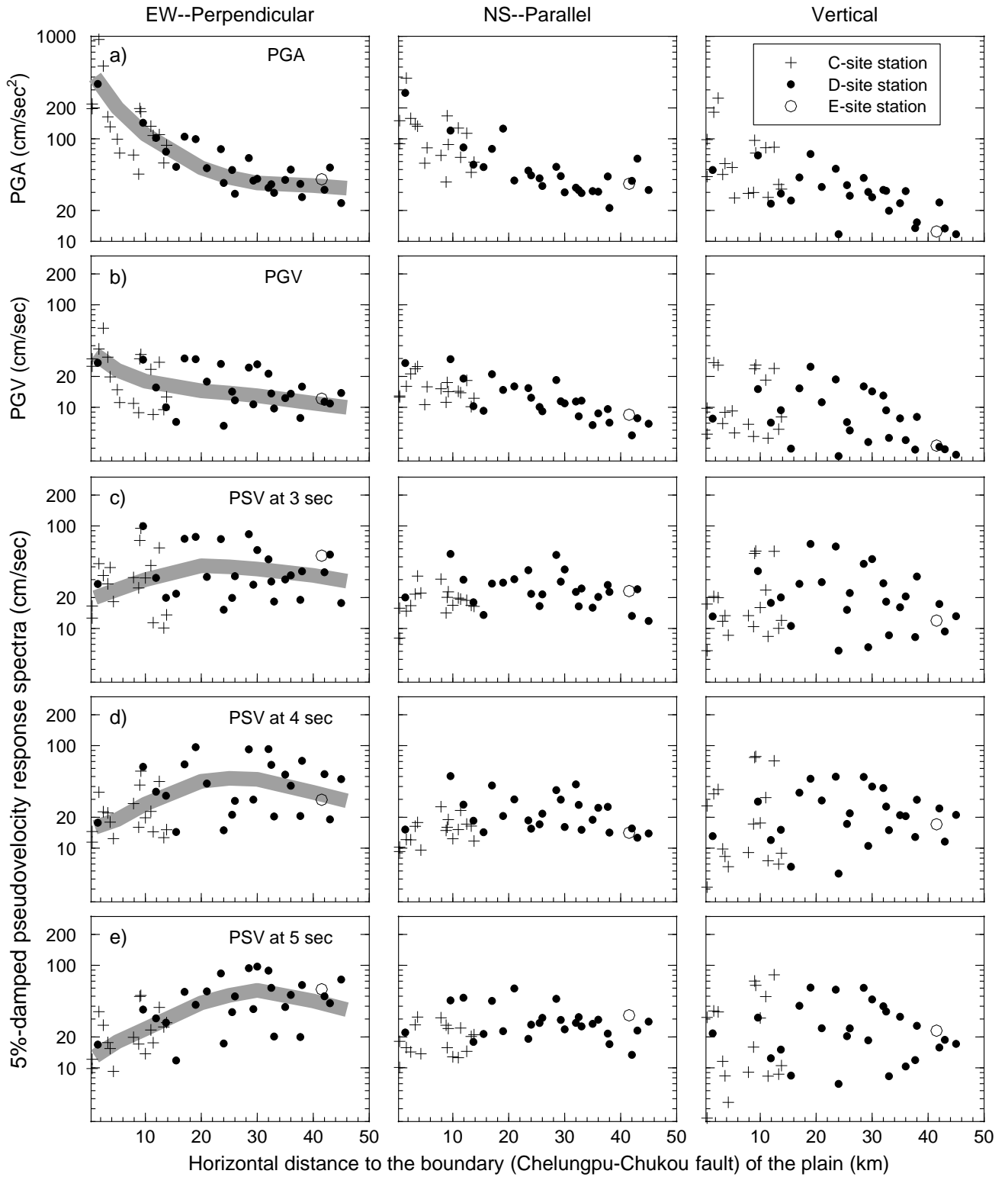


Figure 20: Attenuation of observed ground motions (PGA, PGV, PSV at 3 sec, 4 sec, and 5 sec) in the western Taiwan coastal plain. The main difference between this figure and Figure 19 is that the distance to the boundary ( $R_B$ ), rather than the distance to the source rupture ( $r_{rup}$ ) is used in plotting this figure. Furthermore, data only from 40 stations just opposite to the epicenter are used. The locations of these stations are in the quadrangle marked in Figure 14. To highlight the changes of observed motion with the increment of  $R_B$ , we draw the gray strips manually.

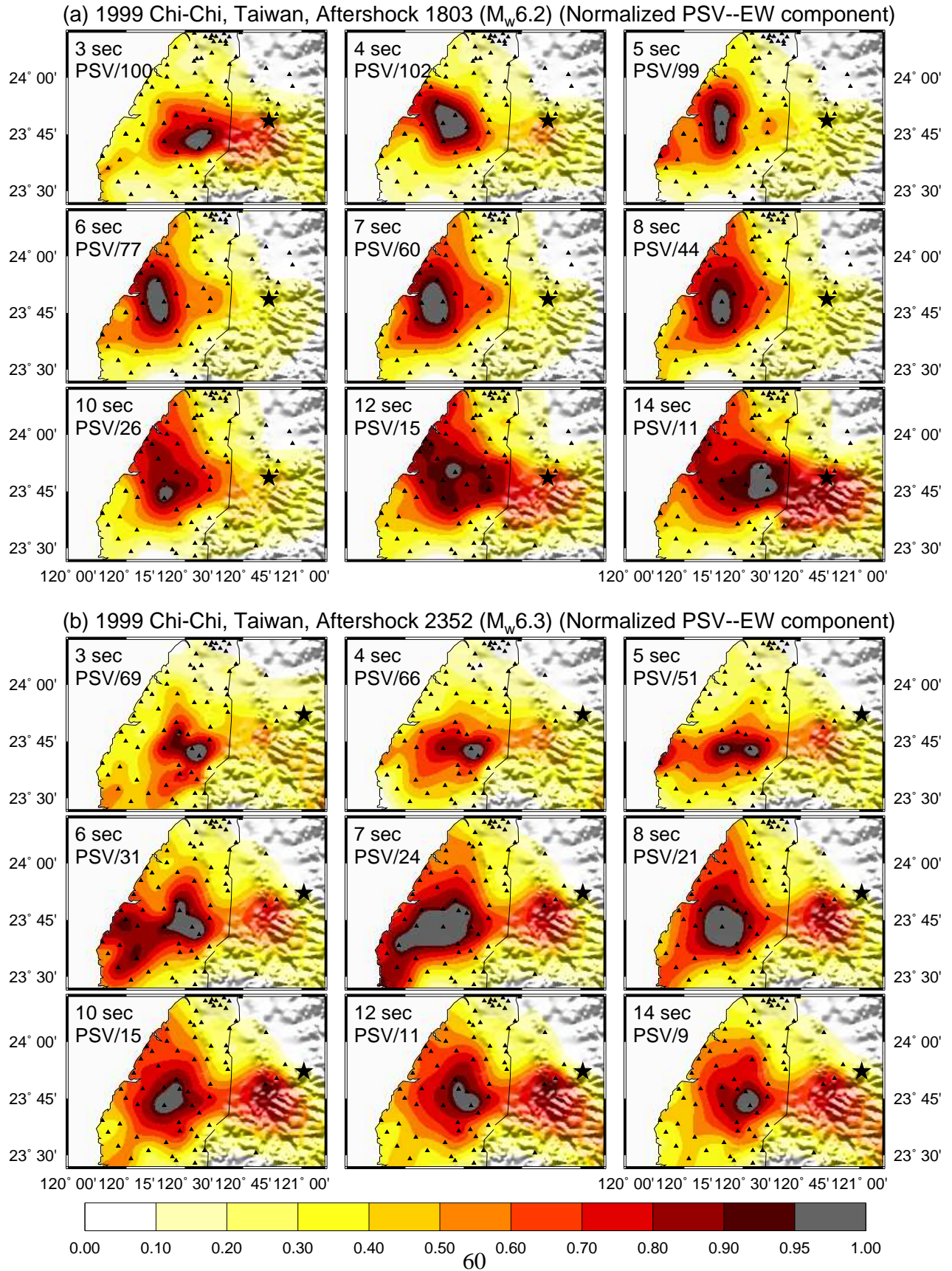


Figure 21: Maps showing spatial distributions of pseudovelocity (PSV) response spectra at periods from 3 sec to 14 sec calculated from the observed strong ground motion records (EW component) during aftershocks 1803 and 2352. The large stars represent the location of epicenters. The small triangles represent stations whose records are used in plotting the contour maps.

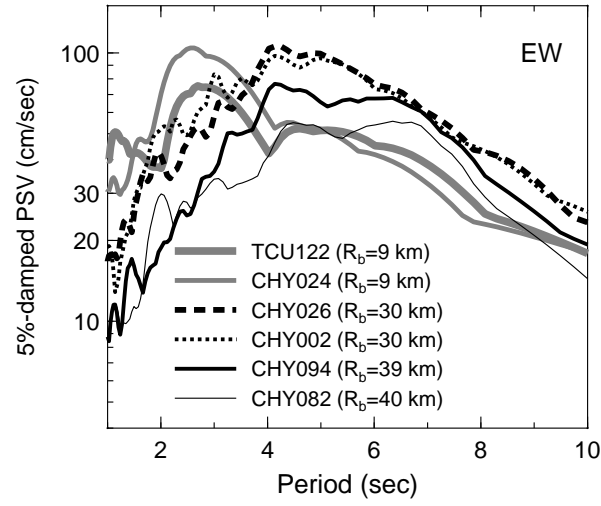


Figure 22: 5%-damped pseudovelocity (PSV) response spectra from six stations (Three groups: [1] TCU122 and CHY024,  $R_B = 9$  km; [2] CHY026 and CHY002,  $R_B = 30$  km; [3] CHY094 and CHY082,  $R_B = 40$  km). The locations of these stations are marked in Figure 3.